PROTEUS

A Physically Realistic Contrast-Enhanced Ultrasound Simulator—Part I: Numerical Methods

Blanken, Nathan; Heiles, Baptiste; Kuliesh, Alina; Versluis, Michel; Jain, Kartik; Maresca, David; Lajoinie, Guillaume

DOI
10.1109/TUFFC.2024.3427850

Publication date
2024

Document Version
Final published version

Published in
IEEE Transactions on Ultrasonics, Ferroelectrics, and Frequency Control

Citation (APA)
Blanken, N., Heiles, B., Kuliesh, A., Versluis, M., Jain, K., Maresca, D., & Lajoinie, G. (2024). PROTEUS: A Physically Realistic Contrast-Enhanced Ultrasound Simulator—Part I: Numerical Methods. *IEEE Transactions on Ultrasonics, Ferroelectrics, and Frequency Control*, *72 (2025)*(7), 848-865. https://doi.org/10.1109/TUFFC.2024.3427850

PROTEUS: A Physically Realistic Contrast-Enhanced Ultrasound Simulator—Part I: Numerical Methods

Nathan Blanken, Baptiste Heiles, Alina Kuliesh, Michel Versluis, *Member, IEEE*, Kartik Jain, David Maresca, and Guillaume Lajoinie, *Member, IEEE*

***Abstract*—Ultrasound contrast agents (UCAs) have been used as vascular reporters for the past 40 years. The ability to enhance vascular features in ultrasound images with engineered lipid-shelled microbubbles has enabled breakthroughs such as the detection of tissue perfusion or super-resolution imaging of the microvasculature. However, advances in the field of contrast-enhanced ultrasound are hindered by experimental variables that are difficult to control in a laboratory setting, such as complex vascular geometries, the lack of ground truth, and tissue nonlinearities. In addition, the demand for large datasets to train deep learning-based computational ultrasound imaging methods calls for the development of a simulation tool that can reproduce the physics of ultrasound wave interactions with tissues and microbubbles. Here, we introduce a physically realistic contrast-enhanced ultrasound simulator (PROTEUS) consisting of four interconnected modules that account for blood flow dynamics in segmented vascular geometries, intravascular microbubble trajectories, ultrasound wave propagation, and nonlinear microbubble scattering. The first part of this study describes the numerical methods that enabled this development. We demonstrate that PROTEUS can generate contrast-enhanced radio-frequency (RF) data in various vascular architectures across the range of medical ultrasound frequencies. PROTEUS offers a customizable framework to explore novel ideas in the field of contrast-enhanced ultrasound imaging. It is released as an open-source tool for the scientific community.**

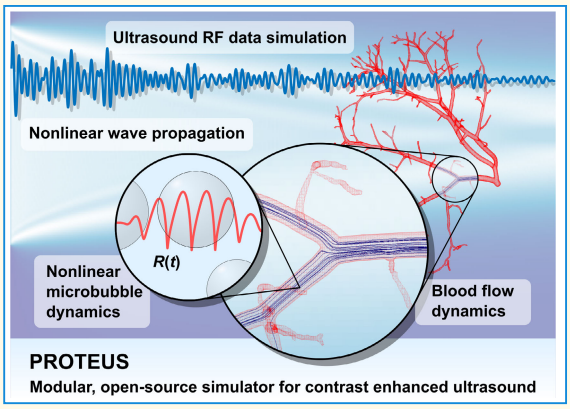

***Index Terms*— Blood flow measurement, multiphysics simulation, nonlinear wave propagation, open-source software, ultrasound contrast agents (UCAs), ultrasound imaging.**

Manuscript received 15 May 2024; accepted 9 July 2024. Date of publication 15 July 2024; date of current version 1 July 2025. This work was supported by SURFSara through NWO under Grant 2019/ENW/00768083 and Grant 2022/ENW/01266133. The work of Baptiste Heiles was supported in part by the 4TU Precision Medicine Program and in part by the Marie-Sklodowska Curie Fellowship of European Union under Grant MIC-101032769. The work of Alina Kuliesh was supported by the TU Delft AI Initiative. The work of David Maresca and Guillaume Lajoinie was supported by the 4TU Precision Medicine Program through High Tech for a Sustainable Future, a framework commissioned by the four technical universities of The Netherlands. The work of Guillaume Lajoinie was supported by European Union (ERC-2022-STG Super FALCON) under Project 101076844. *(Nathan Blanken, Baptiste Heiles, and Alina Kuliesh contributed equally to this work.) (Corresponding authors: Kartik Jain; David Maresca; Guillaume Lajoinie.)*

Nathan Blanken, Michel Versluis, and Guillaume Lajoinie are with the Physics of Fluids Group, Technical Medical (TechMed) Centre, University of Twente, 7522 NB Enschede, The Netherlands (e-mail: g.p.r.lajoinie@utwente.nl).

Baptiste Heiles, Alina Kuliesh, and David Maresca are with the Department of Imaging Physics, Delft University of Technology, 2628 CD Delft, The Netherlands (e-mail: d.maresca@tudelft.nl).

Kartik Jain is with the Department of Thermal and Fluid Engineering, Faculty of Engineering Technology, University of Twente, 7522 NB Enschede, The Netherlands (e-mail: k.jain@utwente.nl).

Digital Object Identifier 10.1109/TUFFC.2024.3427850

I. Introduction

ULTRASOUND is a cost-effective and safe clinical modality used in daily practice to assess the anatomy and function of organs. Patients with impaired vascular conditions are often first diagnosed with ultrasound angiography techniques. In recent years, ultrasound Doppler imaging has become increasingly sensitive owing to the development of ultrasound imaging at kilohertz frame rates [1], [2], [3]. However, Doppler-based approaches remain inherently limited in terms of directional sensitivity, absolute flow quantification, and contrast-to-noise ratio for small-velocity flows.

Blood echogenicity can be increased significantly with intravascular ultrasound contrast agents (UCAs). Clinically approved UCAs consist of polydisperse phospholipid-coated microbubble suspensions with sizes (1–10 μm) similar to those of red blood cells [4], [5]. Microbubbles can resonate, provided that their size matches the transmitted ultrasound frequency, which further enhances their echogenicity. In addition, resonant microbubbles are also nonlinear scatterers even at low acoustic pressure [6]. The nonlinear spectral content of

Highlights

- **PROTEUS is an open-source multiphysics simulator that can generate physically realistic RF data for contrast ultrasound imaging.**
- **PROTEUS integrates computational fluid dynamics in real vasculature, nonlinear wave propagation, and nonlinear microbubble physics in a user-friendly graphical user interface.**
- **PROTEUS provides a unique solution to accelerate the development of emerging ultrasound contrast imaging techniques and to assess their performance quantitatively.**

microbubble echoes, which can exhibit multiples and fractions of the transmitted ultrasound frequency, is exploited by ultrasound pulse sequences to image microbubbles with high specificity in deep tissue to reveal the anatomy of the vasculature or the perfusion degree of a lesion or organ [7], [8], [9], [10], [11].

UCAs thus have a crucial role to play in the future of diagnostic ultrasound and, more generally, in that of biomedical diagnosis. In recent years, advances in contrast-enhanced ultrasound have mostly followed three research directions. The first involves improving contrast agents themselves, for example, by controlling their size distribution [12], [13], [14] or by modifying their shells [15], [16]. Another example is that of so-called gas vesicles (GVs) [17]. These entirely new contrast agents have recently been introduced as the "green fluorescent protein (GFP) for ultrasound" and are being developed as vascular reporters [18]. The second direction concerns new imaging strategies. This involves developing new pulse sequences to exploit nonlinear microbubble contrast and reveal vascular information of interest with higher specificity [19], [20] or advanced postprocessing schemes such as particle image velocimetry (PIV) analysis to enable vector flow imaging (also referred to as echoPIV) [21], [22], [23], [24]. The third direction sets out to break the diffraction limit in vascular imaging. By localizing individual microbubbles in the circulation and reducing the size of their point spread functions (PSFs) by an order of magnitude, ultrasound localization microscopy (ULM) can resolve targets down to a 10-μm resolution in two [25] and three dimensions [26].

The experimental development of contrast-enhanced ultrasound imaging techniques is time and resource-intensive. It often remains difficult to get an objective account of in vivo performance due to the lack of ground truth. Therefore, there is a dire need for accurate simulation tools for hemodynamics, acoustics, and microbubble behavior to benchmark the different steps involved in these approaches. Furthermore, the success of newer approaches based on machine learning depends on the generation of realistic training data [27], [28], [29].

Several simulation tools have been developed to investigate specific aspects of medical ultrasound imaging. To our knowledge, there are two closed-source acoustic simulators: Field II (linear acoustics) [30], [31] and the Verasonics Vantage Ultrasound Simulator (linear acoustics, Verasonics, Kirkland, WA, USA), and five open-source acoustic simulators: k-Wave (full nonlinear acoustics solver) [32], CREANUIS (nonlinear acoustics via the angular spectrum method) [33], [34], SIMUS (linear acoustics) [35], FLUST (linear interpolated) [36], and mSOUND [37]. These tools have been used to simulate contrast-enhanced ultrasound imaging data. Heiles et al. [38] have used the Verasonics simulator in combination with a Poiseuille flow model, disregarding nonlinear acoustics, nonlinear microbubble behavior, and realistic flow patterns. BUbble Flow Field [39] can simulate the nonlinear microbubble response with the Marmottant model and uses a simplified flow representation (Hagen–Poiseuille model) but does not account for nonlinear ultrasound propagation. While the model can generate complex branching structures, these are not derived from in vivo vasculature. Belgharbi et al. [40] use SIMUS and complex in vivo vasculatures that are then reduced to a graph representation. In their approach, flow is represented by a Poiseuille parabolic profile and nonlinear ultrasound propagation as well as nonlinear microbubble scattering are neglected. In order to advance contrast-enhanced ultrasound imaging, there is a need for tools that can accurately simulate the output of an ultrasound imaging transducer, account for ultrasound wave propagation in three dimensions, and model nonlinear microbubble scattering. In addition, an ideal contrast-enhanced ultrasound simulation tool should reproduce physiological blood flow conditions in realistic microvascular networks. None of the tools developed to date fulfill these criteria.

Here, we introduce a physically realistic contrast-enhanced ultrasound simulator (PROTEUS) consisting of four interconnected modules. The first module is a lattice Boltzmann flow solver to simulate blood flow in segmented vascular structures [41], [42]. The second is a microbubble trajectory module to simulate the motion of microbubbles in the flow field. The third is an acoustic module built on top of the wave propagation simulation toolbox k-Wave [32] to simulate arbitrary transducer arrays, ultrasound pulse sequences, and nonlinear wave propagation. The fourth module is an ordinary differential equation (ODE) solver to simulate nonlinear microbubble dynamics [43]. Together, these modules generate physically realistic contrast-enhanced ultrasound radio-frequency (RF) data that can be used to benchmark contrast-enhanced ultrasound imaging.

PROTEUS is an open-source MATLAB application with a graphical user interface that is freely available at https://github.com/PROTEUS-SIM/PROTEUS. For instructions on how to install and use the program, the reader is referred to the documentation in the GitHub repository.

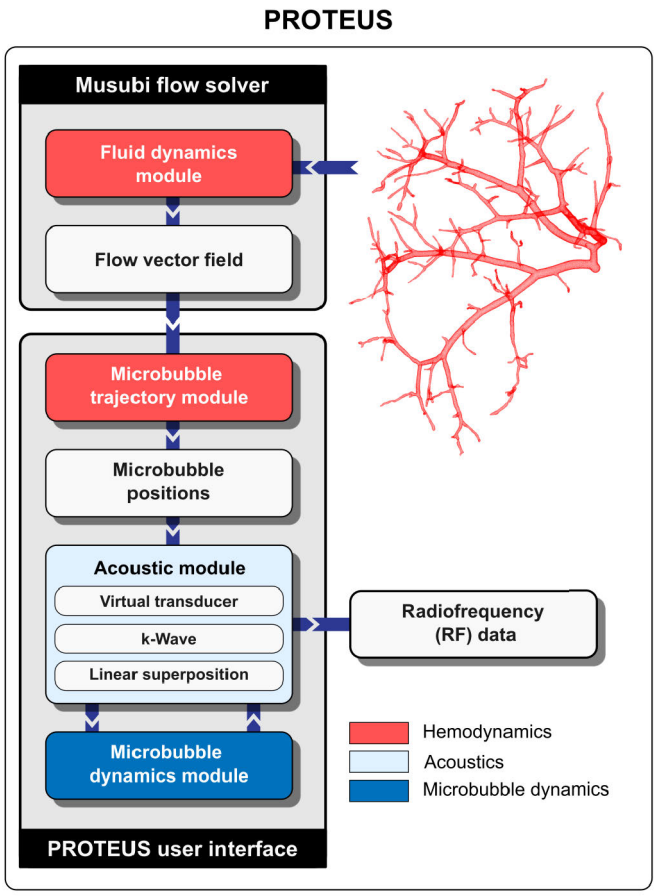

Fig. 1. PROTEUS simulator architecture. Four interconnected simulation modules are used to capture the physics of contrast-enhanced ultrasound and generated simulated contrast-enhanced ultrasound RF data.

II. Modular Simulator Architecture

Fig. 1 shows the connections between the four modules of PROTEUS. The fluid dynamics module computes the flow field in a selected vascular geometry. The microbubble trajectory module processes the output of the fluid dynamics module by computing intravascular microbubble trajectories and outputs the microbubble positions for each transmit pulse in a user-defined imaging sequence. The acoustic module comprises a *virtual transducer* (an accurate representation of a medical transducer as a set of discrete source and sensor points), a propagation medium in which the vascular geometry and the microbubbles are embedded, a nonlinear wave propagation submodule (k-Wave [32]), and an optional linear wave propagation submodule. The virtual transducer transmits ultrasound waves into the medium, exciting the microbubbles contained within. Subsequently, the microbubble dynamics module computes the radial response of each microbubble to the incident pressure wave. Finally, the acoustic module computes the propagation of the microbubble echoes back to the transducer surface and the virtual transducer converts the pressure signals to RF data (voltage signals). This synthetic RF data can then be beamformed to reconstruct ultrasound images. The microbubble trajectory module, the acoustic module, and the microbubble module can be controlled via a graphical user interface that is provided with PROTEUS.

TABLE I
Details of the Presimulated Flow Data

Case	Mean inflow velocity, $\bar{u}$ (cm/s)	Δx (μm)	Δt (μs)	Mesh elements	Smallest & Largest diameters
Renal vasculature	1	60	40	20×10^6	185/420 μm
Brain arteriole	0.5	128	10	68×10^6	3.7/14.2 μm
Cylindrical pipe	35	100	15	49×10^6	20/20 mm

The acoustic module includes two alternative pipelines to compute the microbubble echoes. The *numerical* acoustic simulation pipeline relies entirely on numerical simulations to compute the wave propagation and accounts for both microbubble–microbubble interactions and microbubble–tissue interactions (scatter and attenuation). The *semi-analytical* pipeline was designed to minimize the computation time and computes microbubble–microbubble interactions and microbubble scatter backpropagation with analytical solutions to the wave equation assuming dissipative propagation in a homogeneous medium. The underlying assumptions and theoretical justification are provided in Sections V-C and V-D.

III. Fluid Dynamics Module

A. Musubi Implementation of the Lattice Boltzmann Method

Fluid flow, when treated like a continuum, can be described by the Navier–Stokes equations (NSEs)

$$\frac{\partial}{\partial t}(\rho u_i) + \sum_{j=1}^{3}\left[\frac{\partial}{\partial x_j}\left(\rho u_i u_j\right) - \frac{\partial \sigma_{ij}}{\partial x_j}\right] - \rho g_i = 0 \quad \forall(\vec{x}, t) \tag{1}$$

where x_i and u_i are the fluid displacement and velocity components, respectively; ρ is the fluid density; g is the gravitational acceleration; and σ_{ij} is the stress tensor. We have employed the Einstein summation convention for conciseness. For an incompressible flow, an additional condition for a divergence-free velocity field is imposed

$$\sum_{j=1}^{3}\frac{\partial u_j}{\partial x_j} = 0. \tag{2}$$

PROTEUS employs the fluid dynamics module *Musubi* [41], [42] for the simulation of hemodynamics in arbitrary anatomical geometries. *Musubi* implements the lattice Boltzmann method (LBM) for the numerical solution of the NSE. LBM has its roots in the kinetic theory of gases and recovers the NSE under continuum limits of low Mach and Knudsen numbers. Because of the explicit nature of the scheme, the LBM scales flawlessly on massively parallel computing architectures and has the distinct advantage of being able to represent complex anatomical structures with relative ease compared to finite element or finite volume methods [44]. LBM, due to its strict control of numerical viscosity, allows for direct numerical simulations (DNSs) of physiological flows,

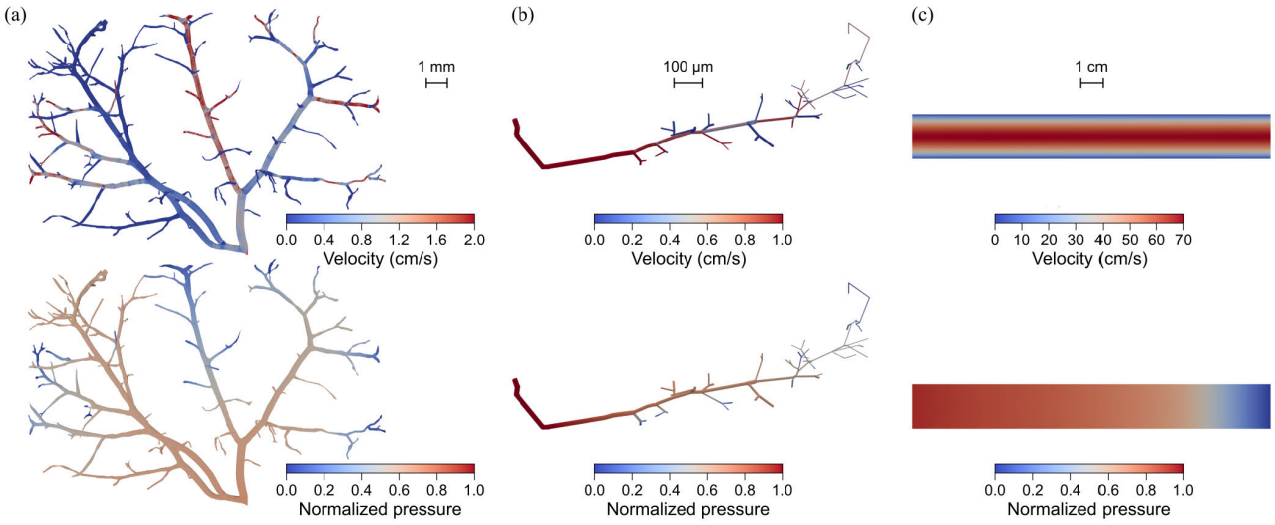

Fig. 2. Precomputed fluid dynamics simulations. Top row: flow velocities. Bottom row: normalized pressures. (a) Rat renal vasculature branch. Flow velocities and normalized pressure behind the vessel wall. (b) Mouse brain arteriole. Flow velocities and normalized pressure behind the vessel wall. (c) Macroscopic cylindrical pipe. Flow velocities and normalized pressure on a diametric cross section.

eliminating the need for turbulence closure models. The LBM is based on the mesoscopic representation of movement of fictitious particles, which have discrete velocities and collide and stream to relax toward a thermodynamic equilibrium. Evolution of the particles over time is described by the lattice Boltzmann equation with the Bhatnagar–Gross–Krook (BGK) collision operator (Ω)

$$f_i(\mathbf{r} + \mathbf{c}_i \Delta t, t + \Delta t) = f_i(\mathbf{r}, t) + \Omega\left(f_i^{\text{eq}}(\mathbf{r}, t) - f_i(\mathbf{r}, t)\right) \quad (3)$$

where f_i represents the density distributions of particles moving with discrete velocity $\mathbf{c}_i$ at a position $\mathbf{r}$ at time t. The Cartesian grid elements in the LBM algorithm are referred to as *stencil*, which contains an arrangement of discrete lattice velocities used to approximate the fluid flow field within a computational domain. The stencil represents the set of discrete velocity vectors that are associated with each lattice node or cell in the computational grid. The indices that run from $i = 1, \ldots, Q$ denote the links per element, i.e., the discrete directions, depending on the chosen stencil. The simulations within this contribution have been performed using the D3Q19 stencil, while *Musubi* implements the D3Q27 stencil as well. Here, the numbers after D and Q refer to the dimensions (3 in this case) and discrete velocity links (19 in this case), respectively. The collision operator Ω defines relaxation of various modes of the distribution functions f_i toward an equilibrium f_i^{eq}

$$f_i^{\mathbf{eq}} = w_i \rho \left(1 + \frac{\mathbf{c}_i \cdot \mathbf{u}}{c_s^2} - \frac{\mathbf{u}^2}{2c_s^2} + \frac{1}{2}\frac{(\mathbf{c}_i \cdot \mathbf{u})^2}{c_s^4}\right) \quad (4)$$

where w_i are the weights assigned to each discrete link in order to ensure that f_i^{eq} satisfies isotropy, Galilean invariance, and stability; and c_s represents the lattice speed of sound, which is proportional to the fluid velocity $\mathbf{u}$. The time step in LBM is coupled with the grid size by $\Delta t \sim \Delta x^2$ due to *diffusive* scaling [45], which is employed to recover the incompressible NSE. Details on the computation of macroscopic quantities from LBM can be found elsewhere [46].

Musubi is a part of the end-to-end parallel simulation framework Adaptable Poly Engineering Simulator (APES), which is available at https://github.com/apes-suite. *Musubi* leverages hybrid parallelization using the message-passing interface (MPI) and open multiprocessing (OpenMP). It has demonstrated excellent scalability on major supercomputers in Germany, Japan, Switzerland, and The Netherlands [41], [47], [48], which allows for accelerated simulations of physiologic flows in complex geometries. *Musubi* has been extensively validated against a number of standard test cases as well as physiological applications [48], [49]. A surface mesh representing vascular geometries is used as a boundary to perform flow computations. A volume mesh is created by the mesh generator *Seeder* and computations are carried out on it using *Musubi*. The inflow boundary condition can be prescribed as either a stationary or pulsatile inflow.

B. Provided Vasculatures

PROTEUS comes with three predefined vasculatures. Alternatively, users can define their own vasculature and flow. The exact procedure to do so is given in the README file on GitHub (https://github.com/PROTEUS-SIM/PROTEUS, Section "New geometries and flow simulations"). The first vasculature included in PROTEUS is a preglomerular renal arterial tree obtained from [50] While the original data provided by Nordsletten et al. [50] contain arterial and venous trees, we included only a part of the arterial tree for simplicity. The second vasculature is a penetrating arteriole in a mouse brain, obtained from [51]. The third is a cylindrical pipe with a 2-cm-diameter featuring Poiseuille flow. By inclusion of the fluid dynamics module Musubi, PROTEUS also offers the possibility to run new hemodynamic simulations, either with the same vascular architectures but with different flow boundary conditions or with any other vascular architecture for which a surface mesh in STL format is available.

Table I lists the inflow boundary conditions, spatial (Δx) and temporal (Δt) resolutions, and the resulting number of mesh elements for each of the three presimulated cases.

A zero-pressure condition is enforced at the outflow boundaries. Blood is described as a Newtonian fluid with a fixed density of 1056 kg/m^3 and a fixed kinematic viscosity of 3.27×10^{-6} m^2/s and is not affected by the presence of bubbles; we do not explicitly model microbubbles as deformable particles in this representation. For the Poiseuille flow in the pipe, we validated the pressure and velocity computations against analytical results. Extensive mesh convergence studies were performed on the renal and brain vasculatures. The data provided with the module contains meshes with a converged accuracy of about second order with respect to the grid resolution.

In the examples presented in this article, we have executed the simulations on 1024 CPU cores of the *Snellius*, a Dutch national supercomputer. Simulating one physical second required about 2.5, 1.2, and 2.2 h for the renal vasculature, the brain arteriole, and the cylindrical pipe, respectively. It should be noted that the *Musubi* LBM solver is based on the octree mesh structure [41], [42], which is mapped into an *unstructured* mesh in VTK. Despite the fact that the LBM mesh appears structured due to its Cartesian topology, the data structures behind it have a noncontiguous coordinate system, which cannot leverage the structured VTK library (Visualization Toolkit [52], legacy format). They are therefore stored in the VTU format (Visualization Toolkit unstructured grid). Fig. 2 shows the velocity and pressure profiles in the three simulated vascular architectures. PROTEUS allows users to import custom geometries and computational fluid dynamics simulations. The procedure to do so is detailed in the GitHub of PROTEUS.

IV. Microbubble Trajectory Module

A. Streamline Computation

The microbubble trajectory module uses the flow data (VTU) from the fluid dynamics module to compute the microbubble positions for each transmit pulse in a user-defined imaging sequence. The VTU file is imported into MATLAB using the MEX interface *vtkToolbox* [53]. Although we designed PROTEUS to work with the flow solver *Musubi*, any flow data in VTU format could be imported into the microbubble trajectory module, provided that the volume mesh has a Cartesian topology.

The transmit sequence is defined by the number of frames, the frame rate, the pulsing scheme (Section V-A), and the time between the pulses that constitute a frame. As the flow velocity is typically much smaller than the speed of sound, we assume that the microbubbles are stationary during transmission of a pulse and the subsequent scattering.

We assume that microbubble trajectories are unaffected by acoustic radiation forces such as Bjerknes forces [54], [55] and the microbubbles follow the streamlines of the flow. The streamlines are computed by integrating the flow velocity using the MATLAB ODE23 solver. To ensure the accuracy, the maximum integration time step was set to $2d_{\mathrm{VTU}}/u_{95}$, where d_{VTU} is the cell size of the flow simulations and u_{95} is the 95th-percentile velocity. This upper bound limits the maximum travel distance of a microbubble to two simulation cells between time steps. In practice, the time steps are optimized by the ODE solver itself, and this limit has been shown to be sufficient by comparison to established algorithms; our streamline integration method was validated against a reference method implemented in the module PyVista [56].

During the entire imaging sequence, the number of microbubbles N_{MB} inside the vascular geometry is kept constant. For the first acquisition, N_{MB} microbubbles are distributed randomly throughout the volume of the vascular geometry. Next, the trajectories of these microbubbles are computed. When a microbubble exits the vasculature at an outlet boundary, the microbubble trajectory module creates a new microbubble at a random position on the inlet surface and propagates it from there [Fig. 3(a)].

B. Inlet Probability Density

The probability for a microbubble to enter through a specific point on the inlet surface is a boundary condition that depends on the details of the flow in the vessels outside the segmented geometry. We therefore cannot provide a physically realistic inlet distribution. Instead, PROTEUS provides a probability distribution that ensures good coverage of the vascular geometry with microbubbles. This approach is useful for applications such as ULM, in which it may take a long time to cover all the branches with microbubbles.

We computed this density map by distributing a large number of microbubbles randomly throughout the volume of the vasculature and reversing the flow direction, thereby backpropagating the microbubbles to the inlet. For the rat renal vasculature, we homogeneously distributed 5000 microbubbles throughout the volume of the vasculature and backpropagated them for 10 s, corresponding to an imaging sequence of 5000 frames at 500 Hz. The number of microbubbles was chosen as a compromise between simulation time and coverage. A small fraction (less than 2%) of the microbubbles did not reach the inlet within this integration time as the flow in some branches was restricted [Fig. 2(a)]. The endpoints of the microbubbles that reached the inlet were binned into the cells of the volume mesh that constitute the inlet surface. The resulting 2-D histogram was convolved with a 2-D Gaussian convolution and normalized to yield a smooth probability density map. Microbubbles can then be injected at arbitrary, nondiscrete locations within this inlet. The inlet density map for the rat renal vasculature is shown in Fig. 3(a). Similarly, we have precomputed inlet density maps for the mouse brain arteriole and the macroscopic straight pipe. Fig. 3(b) shows the output of a microbubble trajectory simulation using the precomputed inlet density map for the rat renal vasculature.

C. Microbubble Size Distribution

Each microbubble in the initial microbubble population is assigned a random radius R_0 drawn from a size distribution that can be arbitrarily defined (probability density as a function of radius). Also, each new microbubble that is created at the inlet when a microbubble exits through an outlet is assigned a new random radius from the distribution.

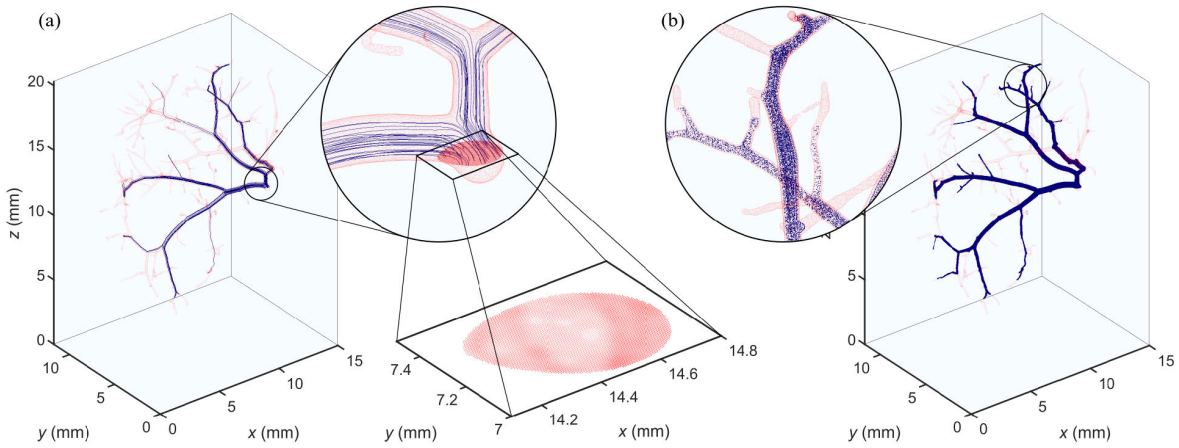

Fig. 3. Microbubble trajectory module. (a) Intravascular trajectories of 50 individual microbubbles originating from the inlet surface of the rat renal vasculature. The dots on the inlet surface represent the centers of the computational cells that constitute the inlet surface. The size of the dots is proportional to the probability that a new microbubble enters through this cell. The probability density within each cell is uniform. (b) Cumulative microbubble positions of 15 microbubbles for 10 000 frames at a frame rate of 100 Hz. When a microbubble reaches an outlet of the vasculature, a new microbubble is inserted at the inlet.

PROTEUS offers three predefined contrast agent types: 1) the commercial contrast agent SonoVue[1] (Bracco Suisse SA, Geneva, Switzerland), filled with sulfur hexafluoride; 2) the preclinical contrast agent BR-14 (Bracco Research, Geneva, Switzerland), filled with perfluorobutane; and 3) monodisperse microbubbles produced using microfluidic techniques [12]. The size distributions of both SonoVue and BR-14 are modeled with a fit to an experimental measurement of the size distribution of BR-14 [57]

$$P = A R_0^2 e^{-a R_0} \tag{5}$$

with $a = 2.19\ \mu\text{m}^{-1}$ and A a normalization factor [28]. The monodisperse distribution is approximated by a Gaussian distribution of which the mean radius and the polydispersity index (PDI, standard deviation radius divided by mean radius) can be arbitrarily defined. Alternatively, the user can load a custom size distribution.

The domain of the size distributions is restricted to radii ranging from 0.5 to 6 μm because microbubbles outside that range typically represent only a negligible fraction, whereas simulating their response with the microbubble trajectory module (Section VI) takes an impractically long time. Moreover, few studies provide insight into the physics of the lipid shells of microbubbles outside that range.

V. Acoustic Module

A. Virtual Transducer

We emulate commercially available transducer arrays based on experimental characterization. The characterization comprises two parts: 1) determination of the transmit and receive impulse responses and 2) pressure field matching by elevation focus and amplitude tuning. The pressure response of the transducer $p_T(t)$ to any input voltage signal $V_T(t)$ can be computed by convolution with the transmit impulse response $h_T(t)$

$$p_T(t) = h_T(t) * V_T(t). \tag{6}$$

Similarly, the voltage response $V_R(t)$ to an incoming pressure wave $p_R(t)$ is computed by convolution with the receive impulse response $h_R(t)$

$$V_R(t) = h_R(t) * p_R(t). \tag{7}$$

The two-way impulse response is $h_{TR} = h_T * h_R$. PROTEUS currently supports the definition of arbitrary 1-D and 2-D arrays where all elements have the same in-plane orientation. These include linear arrays and phased arrays. The effect of the transducer lens is modeled by applying delays along the length of the transducer elements

$$\tau = \left(\sqrt{(L/2)^2 + f_e^2} - \sqrt{y^2 + f_e^2}\right) \Big/ c_0 \tag{8}$$

where L is the length of the transducer elements, f_e is the elevation focal length, y is the spatial coordinate along the length of the transducer elements, and c_0 is the speed of sound. Here, we demonstrate the characterization and modeling of a P4-1 transducer (Philips ATL).

To measure the transmit impulse response, we connected the transducer to a Vantage 256 system (Verasonics, Kirkland, WA, USA) and drove it with an approximation of a Dirac delta pulse (12-ns, 30-V rectangular pulse). With a fiber-optic needle hydrophone (Precision Acoustics, Dorchester, U.K.) positioned close to the elevation focus, we recorded the output pressure. We applied an asymmetric, cosine tapered window to eliminate a 3.3-MHz hydrophone resonance tail and to ensure a smooth transition to zero at the start and end of the signal [Fig. 4(a)]. To determine the receive impulse response, we first measured the two-way impulse response by placing a metal reflector halfway between the transducer and its elevation focus to maximize the received signal amplitude [58], [59]. We applied another asymmetric, cosine tapered window to eliminate reflections resulting from reverberations within the metal plate and to ensure a smooth transition to

[1]Registered trademark.

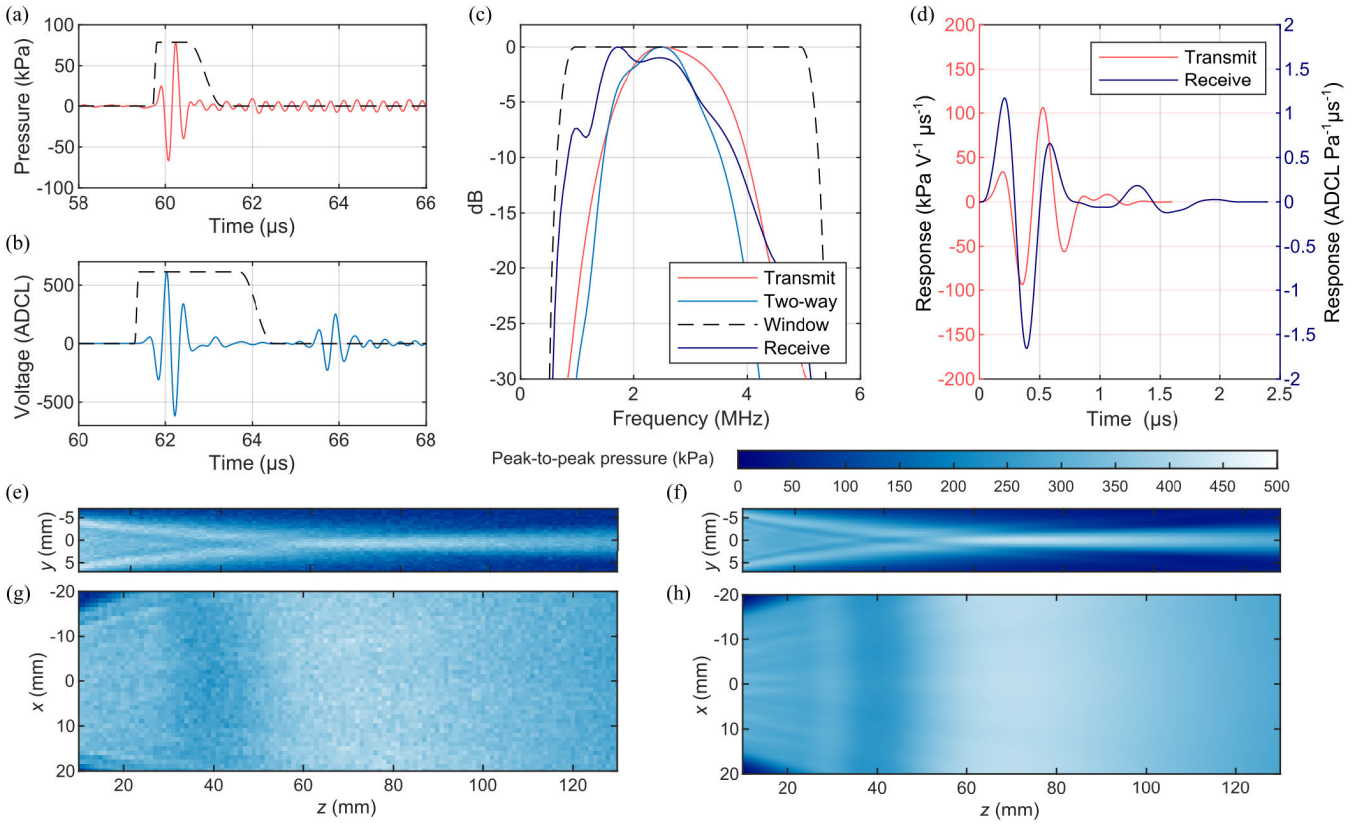

Fig. 4. (a) Impulse response of the P4-1 transducer in transmit measured using an optical hydrophone. (b) Impulse response of the P4-1 transducer in transmit–receive (i.e., two-way) measured using the reflection from a steel plate. The windows in (b) and (c) are applied to remove noise and secondary reflections. ADCL stands for analog-to-digital converter levels. (c) Fourier transform of the impulses responses in (a) and (b). (d) Scaled transmit and receive impulse responses implemented in the simulator. (e) Measured and (f) simulated elevation profiles of the pressure field generated by the P4-1 transducer. (g) Measured and (h) simulated pressure field generated by the P4-1 transducer in the imaging plane.

zero [Fig. 4(b)]. To eliminate any second-harmonic generation caused by nonlinear propagation through the medium, we repeated the procedure with a negative-polarity driving pulse and subtracted the results. We then determined the receive impulse response h_R through division in the Fourier domain. Since $h_{TR}(t) = h_T(t) * h_R(t)$, we have $H_{TR}(f) = H_T(f)H_R(f)$, where $H_T(f)$, $H_R(f)$, and $H_{TR}(f)$ denote the transmit, receive, and two-way transfer functions, respectively (i.e., the Fourier transforms of the respective impulse responses). As a regularization method, we multiplied the ratio $H_{TR}(f)/H_T(f)$ with a cosine tapered window to suppress the sections of the frequency domain with a poor signal-to-noise ratio before conversion back to the time domain [Fig. 4(c)]. Fig. 4(d) shows the resulting receive impulse response.

The transducer source in the simulations is defined as a velocity source at the transducer surface with velocity $u_x(t)$. For a 1-D plane wave, the relation between particle velocity $u_x(t)$ and pressure $p_T(t)$ is $p_T(t) = \rho_0 c_0 u_x(t)$, where ρ_0 and c_0 are the average density and the average speed of sound of the medium, respectively. Although this relation is not true for 3-D waves, we can assume it to be true locally at the transducer surface. Furthermore, we assume that the pressure measured near the elevation focus is proportional to the pressure $p_T(t)$ at the transducer surface. In addition to the unknown amplitude proportionality factor, the location of the elevation focus of the transducer is not precisely known. To determine these parameters, we took two orthogonal, 2-D scans of the transmit field with a fiber-optic needle hydrophone mounted on a three-axis translation stage [see Fig. 4(e) and (g)]. Next, the transmit impulse response amplitude and the elevation focus were tuned iteratively until reaching an on-axis root-mean-square difference between simulation and experiment of less than 7% of the maximum amplitude, which is about the noise level in the experimental pressure map [see Fig. 4(f) and (h)]. Note that the impulse response and the elevation focus are intrinsic properties of the transducer, which only need to be determined once and do not need to be adjusted when using other waveforms or beam profiles.

The wave transmit simulations rely on k-Wave simulations, which are grid-based. To map the continuous transducer surface onto the grid, the continuous source distribution is convolved with a band-limited delta function. This procedure is described in more detail in Section V-E.

The user interface of PROTEUS provides two preset transmit voltage types: three-state and sinusoidal. These signal types model switched and linear transmitters. The center frequency and the number of cycles can be arbitrarily defined. Alternatively, fully custom voltage signals can be loaded into the user interface. The lateral focus, steer angle, and element apodization (which can be positive and negative) can also be modified to simulate a multitude of beam profiles.

In addition to single-pulse plane-wave imaging, PROTEUS provides three multipulse schemes for nonlinear signal detection: single pulse (standard), pulse inversion (PI), amplitude

modulation (AM), and amplitude-modulated pulse inversion (AMPI) [11]. The AM and AMPI pulsing schemes are implemented with *checkerboard apertures*, which are a common technique used in practice to avoid the difficulties involved in rapidly switching the transmit amplitude [11]. Although PROTEUS does not provide predefined multiplane sequences such as coherent compounding [60], these sequences can be simulated by repeating a single-pulse simulation with the same microbubble population, but with different transmit settings.

B. GPU-Accelerated Acoustic Simulation

The interaction of the transmit wave with the microbubbles and microbubble–microbubble crosstalk (multiple scattering) is simulated by iterative communication between the acoustic module and the microbubble dynamics module (Section VI). The acoustic module comprises two alternative pipelines to compute the microbubble echoes (Fig. 5). The *numerical* acoustic simulation pipeline relies entirely on numerical simulations to simulate the wave propagation (indicated by the letter K in Fig. 5). The *semi-analytical* pipeline was designed to minimize the computation time and relies both on numerical simulations (K) and analytical solutions to the wave equation (indicated by the letter L in Fig. 5). The numerical and the semi-analytical pipelines will be detailed in Sections V-C and V-D, respectively. In this section, we describe the common functionality of the two pipelines.

During its first iteration, the acoustic module simulates the wave propagation from the transducer into the medium. To account for attenuation, nonlinear propagation, and medium inhomogeneity, the acoustic module uses a k-Wave simulation [32], [61] to compute the 3-D forward wave propagation. Each of the microbubble positions computed with the microbubble trajectory module is incorporated into the medium as pressure sensors [top left block of Fig. 5(a)].

The propagation medium consists of a tissue in which the vessel architecture is embedded. The tissue is defined by the speed of sound (c_0), the density (ρ_0), a nonlinearity parameter (B/A), and attenuation. The dependence of the attenuation on frequency is modeled by a power law [62]. The graphical user interface of PROTEUS contains a list of predefined tissues with properties extracted from literature: generic soft tissue, fat tissue, kidney tissue, brain tissue, water, and blood [63]. Alternatively, the graphical user interface allows for custom definition of the tissue properties. The vessel lumen can be filled with blood or water. Note that this choice determines the acoustic properties but not the fluid dynamics simulation (Section III) as the latter is external to the user interface (Fig. 1). To embed the vascular geometry into the k-Wave grid, the surface mesh (STL file) is converted to a voxel representation using the MATLAB mesh voxelization toolbox (File Exchange 27390), which uses a ray intersection method [64]. In the user interface of PROTEUS, the vascular geometry can be placed at an arbitrary distance from the transducer with an arbitrary orientation.

In k-Wave, the maximum frequency supported by the computational grid is given by the Nyquist sampling limit [61]. This limit can be expressed as $f_{\max} = n_{\text{ppw}} f_0/2$, where f_0 is the center frequency of the transmit waveform and n_{ppw} is the number of grid points per wavelength λ, with λ the wavelength at the center frequency. The number of grid points per wavelength n_{ppw} can be set in the user interface. The choice of n_{ppw} determines which higher harmonics (resulting from nonlinear propagation or nonlinear microbubble behavior) can be simulated. For example, the highest frequency in the third harmonic is about $4f_0$ ($3f_0$ center frequency and f_0 margin for the bandwidth of the signal). To capture the third harmonic, a grid spacing of $\lambda/8$ should be specified. Such a high resolution can result in large grids ($\sim 10^8$ grid points). To minimize the computation time, k-Wave provides precompiled C++/CUDA code to run simulations on a GPU. In Section VII-B, we analyze the computation times of PROTEUS.

In order to mimic the speckle generated by tissue, the speed of sound and the density of each grid point are modulated by Gaussian random noise. The scattering strength of the tissue can be adjusted by changing the standard deviation value of this random noise in the user interface.

The pressure recorded by the microbubbles serves as input to the microbubble dynamics module, which computes the radial oscillations $R(t)$ of each individual microbubble. In the next iteration of the acoustic module, the microbubbles act as both pressure sensors and mass sources, which represent the mass injection rate per unit volume [65]. Since the microbubbles are much smaller than the wavelength of the ultrasound, they can be considered as point sources. Therefore, the mass injection rate of a microbubble is given by

$$S_{\text{M}}(\mathbf{r}, t) = \rho_{\text{L}} \dot{V}(t) \delta^3(\mathbf{r}) = 4\pi \rho_{\text{L}} R^2 \dot{R} \delta^3(\mathbf{r}) \tag{9}$$

where ρ_{L} is the density of the liquid in the vessel, $\dot{V}(t)$ is the rate of change of the microbubble volume, and the $\mathbb{R}^3$ Dirac delta $\delta^3(\mathbf{r})$ represents a point source distribution ($\mathbf{r} \in \mathbb{R}^3$). This iteration can be repeated N_{inter} times to account for multiple scattering of order N_{inter}. Multiple scattering is neglected by setting $N_{\text{inter}} = 0$.

In the final k-Wave iteration, for both pipelines, the microbubbles act as sources, and the transducer acts as a sensor. In addition, in the numerical pipeline, the transducer also acts as a source to compute the interaction between the transmit wave and the tissue scatterers. By contrast, the semi-analytical pipeline already computes the tissue scatter during the first k-Wave iteration. The virtual transducer converts the sensor data recorded by the transducer to RF data [Fig. 5(a)] by applying lens delays (8), integrating over the surface of the transducer elements, and convolving the pressure signals with the receive impulse response (7).

For each next frame and each next pulse in the pulse sequence, the microbubble positions are updated and the acoustic simulation procedure is repeated, with the exception of the transmit wave propagation simulations (one such simulation for each pulse in the sequence). Since the microbubbles do not act as sources in these first k-Wave iterations, the computed field is independent of the microbubble positions. Furthermore, the tissue is stationary. Therefore, the first iterations only need to be run once if sensor points are placed at all accumulated microbubble positions from all the frames.

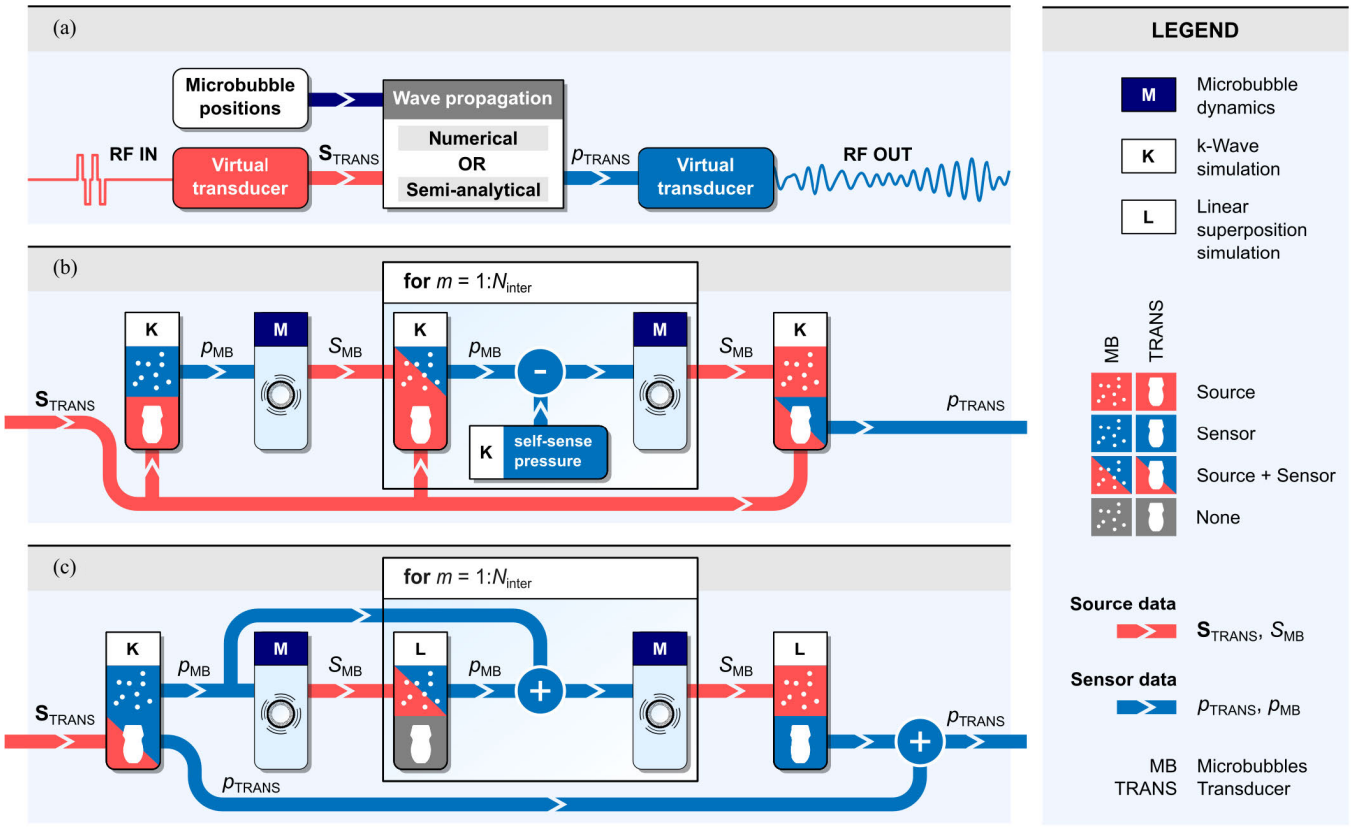

Fig. 5. Acoustic simulation pipeline. (a) Entire pipeline of the acoustic module. (b) Numerical pipeline. (c) Semi-analytical pipeline.

C. Numerical Pipeline

To capture the acoustic interaction of microbubble echoes with heterogeneous tissue, the numerical pipeline uses k-Wave simulations for each iteration of the acoustic module. In k-Wave, point sources are approximated by voxel sources or, more generally, by band-limited source distributions (Section V-E). This approximation is valid if the spacing between sources and sensors is much larger than the grid spacing. Since the mass injection rate defined in (9) is expressed per unit volume, δ^3 must be substituted with $(\Delta x \Delta y \Delta z)^{-1}$, where Δx, Δy, and Δz represent the grid spacing in each dimension (in PROTEUS, $\Delta x = \Delta y = \Delta z$). The mass injection rate for a voxel representation of a microbubble thus becomes

$$S_{\mathrm{M}}(t) = \frac{\rho_{\mathrm{L}}}{\Delta x \Delta y \Delta z}\frac{\partial V}{\partial t} = \frac{4\pi\rho_{\mathrm{L}} R^2(t)}{\Delta x \Delta y \Delta z}\frac{dR}{dt}. \tag{10}$$

Since the source input structure in k-Wave for monopole source distributions (`source.p`) is given in units of pressure, the mass source distribution described by (10) must be converted into a pressure source by rescaling as

$$\texttt{source.p} = \frac{c_0 \Delta x}{2} S_{\mathrm{M}} \tag{11}$$

where c_0 is the speed of sound at the source position.

In the k-Wave iterations that account for microbubble–microbubble interaction [the for-loop block in Fig. 5(b)], the microbubbles act as both sources and sensors. However, the pressure recorded by a specific microbubble also includes the pressure field generated by this microbubble *itself*. This represents a nonphysical situation in which a microbubble is driven by itself. We compute this *self-sense* pressure component by running a small-domain k-Wave simulation only including the microbubble under consideration. By limiting the domain size of this simulation, we keep its contribution to the overall simulation time to a minimum. After subtraction of the self-sense pressure, the sensor data are fed into the next iteration of the microbubble dynamics module.

Due to the high number of user-definable simulation parameters, the execution times of PROTEUS can vary greatly. By inspection of Fig. 5(b), we obtain the following expression for the total execution time T_{sim} for the numerical pipeline:

$$\begin{aligned} T_{\mathrm{sim}} = {} & T_{\mathrm{kW}} N_{t_1} N_{\mathrm{p}} \\ & + N_{\mathrm{f}} N_{\mathrm{p}} \big[T_{\mathrm{MB}} N_{\mathrm{MB}} + N_{\mathrm{inter}} \big(T_{\mathrm{kW}} N_{t_2} + T_{\mathrm{kW}}^{\mathrm{S}} N_{t_2} N_{\mathrm{MB}} \\ & + T_{\mathrm{MB}} N_{\mathrm{MB}} \big) + T_{\mathrm{kW}} N_{t_3} \big] \end{aligned} \tag{12}$$

where T_{kW} is the execution time of k-Wave per time step. Approximately, T_{kW} scales linearly with the total number of spatial grid points. N_{t_1}, N_{t_2}, and N_{t_3} are the number of time steps for the successive k-Wave iterations. $N_{t_3} > N_{t_2} > N_{t_1}$ as the pressure wave needs to travel further in each next iteration. $T_{\mathrm{kW}}^{\mathrm{S}}$ is the execution time of a single small-domain k-Wave run to compute the self-sense pressure. T_{MB} is the execution time required to compute a single microbubble response, which depends on the parameters of the microbubble dynamics module, such as the microbubble size, the driving frequency, and the acoustic pressure. N_{f} is the number of frames and N_{p} is the number of pulses in the pulsing scheme. Note that the

first term is not dependent on N_f as the first k-Wave iteration only needs to be run once for each pulse in the pulsing scheme.

D. Semi-Analytical Pipeline

A major drawback of the numerical pipeline is its computational cost. The simulation pipeline can be substantially accelerated by making two approximations that allow for the replacement of the majority of k-Wave simulations by faster, linear superposition simulations [Fig. 5(c)]. The first approximation is that the scattered waves propagate linearly, which can be justified by the fact that the pressure amplitude of microbubble scatter scales as R_0/r, rapidly dropping to values several orders of magnitude lower than the pressure amplitude of the transmit wave, typically within a few wavelengths. The second approximation is to model the medium as a homogeneous medium for the propagation of the scattered waves (neglecting microbubble–tissue interaction). In Section VII-C, we explore the limits of this approximation. We can therefore use Green's function approach to compute the pressure scattered by the microbubbles, as demonstrated next.

Biological tissue exhibits a power law absorption $\alpha(\omega) = \alpha_0\omega^y$, with α_0 the attenuation coefficient in Np(rad/s)$^{-y}\cdot$m^{-1} and ω the angular frequency of the acoustic wave [62]. The exponent y is typically in the range $1 \leq y \leq 1.5$. Pressure waves p in such power law media can be described by the fractional differential equation

$$\nabla^2 p - \frac{1}{c_0^2}\frac{\partial^2 p}{\partial t^2} - \frac{2\alpha_0}{c_0\cos(\pi y/2)}\frac{\partial^{y+1} p}{\partial t^{y+1}} - \frac{\alpha_0^2}{\cos^2(\pi y/2)}\frac{\partial^{2y} p}{\partial t^{2y}} = -S(\mathbf{r}, t) \quad (13)$$

where c_0 is the (homogeneous) speed of sound in the medium [66]. The Green's function $g(\mathbf{r}, t)$ of this equation is the response to an impulse input $\delta^3(\mathbf{r})\delta(t)$ and can be expressed with the temporal convolution [66]

$$g(r, t) = \frac{\delta(t - r/c_0)}{4\pi r} * \mathcal{F}^{-1}\left\{\exp\left(-\alpha_0 r\left(|\omega|^y + i\tan(\pi y/2)\omega|\omega|^{y-1}\right)\right)\right\} \quad (14)$$

which can alternatively be expressed as $g(r, t) = \mathcal{F}^{-1}\{\hat{g}(r, \omega)\}$, with the material transfer function

$$\hat{g}(r, \omega) = \frac{1}{4\pi r}\exp\left(-\alpha_0 r|\omega|^y - i\omega r/c(\omega)\right) \quad (15)$$

where $\mathcal{F}^{-1}$ denotes the inverse Fourier transform and $c(\omega)$ is the dispersion relation for power law media with even or noninteger powers [62], [67]

$$\frac{1}{c(\omega)} = \frac{1}{c_0} + \alpha_0\tan(\pi y/2)|\omega|^{y-1}. \quad (16)$$

A monopole source term can be expressed as $S(\mathbf{r}, t) = \partial S_M/\partial t$, where $S_M = \rho_L \dot{V}(t)\delta^3(\mathbf{r})$ is the mass injection rate (9). Therefore, the field scattered by a microbubble can be computed with the temporal convolution

$$p(r, t) = \rho_L \ddot{V}(t) * g(r, t) = \rho_L \mathcal{F}^{-1}\left\{\mathcal{F}\left\{\ddot{V}(t)\right\}\hat{g}(r, \omega)\right\}. \quad (17)$$

For lossless media ($\alpha_0 = 0$), (17) reduces to the well-known equation for the scattered pressure of a bubble

$$p(r, t) = \frac{\rho_L R}{r}\left(R\ddot{R} + 2\dot{R}^2\right) * \delta(t - r/c_0). \quad (18)$$

This equation is the same as the one presented by Keller and Kolodner [68], except for a rapidly decaying near-field term $\rho_L(R^2\dot{R})^2/4r^4$, which is not recovered because we represent the microbubbles as point sources. To prevent waves from reappearing at the other side of the time domain due to the periodic nature of the discrete Fourier transform, we expand the time domain by a factor of 2 before evaluating (17). The procedure described above breaks down for $y = 1$ because $\cos(\pi y/2) \to 0$ in the denominator in (13). Currently, we simply disregard dispersion for this case, analogous to k-Wave's approach, by setting $c(\omega) = c_0$. For applications for which modeling dispersion accurately is crucial, the exponent can be set to $y \geq 1.1$. Finally, for each sensor point $\mathbf{r}_n$, we sum the pressure contributions from all microbubbles (linear superposition)

$$p_n(t) = \sum_{m \neq n} \rho_L \mathcal{F}^{-1}\left\{\mathcal{F}\left\{\ddot{V}_m(t)\right\}\hat{g}(r_{mn}, \omega)\right\} \quad (19)$$

where $\ddot{V}_m(t)$ is the volumetric oscillation of microbubble m and $r_{mn} = |\mathbf{r}_n - \mathbf{r}_m|$ is the distance between source m and sensor n. We refer to (15), (16), and (19) collectively as the *linear superposition module*, indicated by L in Fig. 5(c).

For the transmitted waves, nonlinear propagation can typically not be neglected. Therefore, the first iteration in the semi-analytical pipeline, such as for the numerical pipeline, consists of a k-Wave simulation (indicated by the letter K in Fig. 5). This first iteration is the only iteration in which we include a heterogeneous medium to mimic tissue scatter. The transducer must therefore also act as a sensor to capture the tissue scatter. Since the first k-Wave iteration only needs to be run once for all frames (Section V-B), its contribution to the overall simulation time becomes negligible for a large number of frames.

Propagation of the waves scattered by the microbubbles, however, is computed using the linear superposition submodule. Since the wave propagation from the transducer is not included in L, the sensor data from the first iteration (K) are added to the sensor data from L. Unlike the numerical pipeline, the semi-analytical pipeline does not encounter the issue of self-sense pressure, as $m = n$ is excluded from the sum in (19).

The time required to evaluate (19) is negligible compared to the time required to compute the microbubble response. Therefore, the terms in (12) containing T_{kW}, except the first one, can simply be eliminated, yielding the following expression for the total execution time for the semi-analytical pipeline:

$$T_{sim} = T_{kW}N_{t_1}N_p + N_f N_p N_{MB} T_{MB}(1 + N_{inter}). \quad (20)$$

In addition to the increased simulation speed, the semi-analytical pipeline has the added advantage that point sources are not approximated by finite-size voxels. This allows the microbubble sources and sensors to come arbitrarily close, up to the point where the physics of the microbubble dynamics breaks down [69].

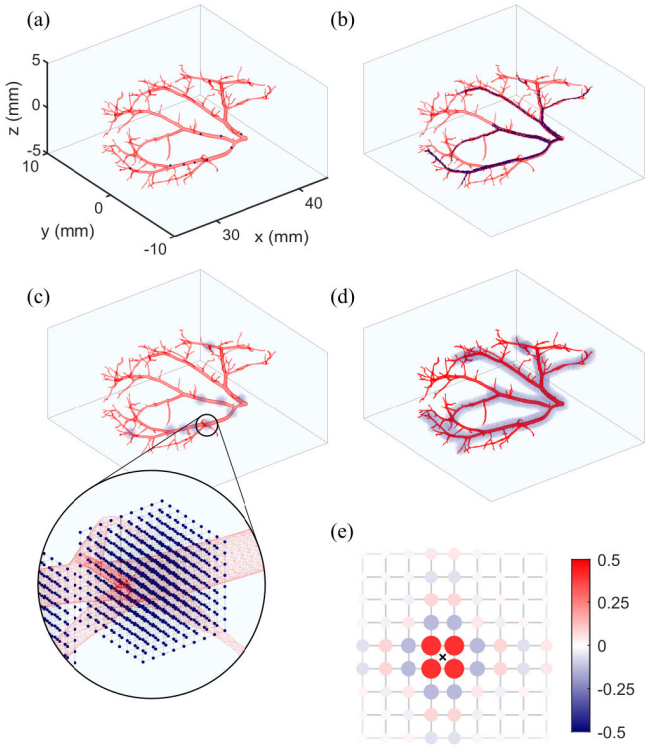

Fig. 6. Placement of sensor points for the on-grid and off-grid microbubble cases. Simulation with ten microbubbles and 1000 frames. (a) On grid, single frame, ten sensor points. (b) On grid, microbubble positions of all frames accumulated, 1614 sensor points. (c) Off grid, single frame, 7269 sensor points. (d) Off grid, microbubble positions of all frames accumulated, 71 707 sensor points. (e) Evaluated band-limited delta function for an off-grid microbubble (on-grid along the out-of-page axis).

E. Implementation of Off-Grid Sources and Sensors

Confinement of sources and sensors to single grid points results in staircase movement of the microbubbles across multiple frames. This unrealistic representation of bubble motion would be crippling for, e.g., super-resolution applications. Recently, a method has been presented to represent an arbitrary, continuous distribution of sources and sensors on a grid [70], which we have incorporated in our simulation framework and which we will briefly describe here.

The method is based on the projection of the delta function onto the band-limited space of the voxel grid. The 3-D delta function $\delta^3(\mathbf{r}, \boldsymbol{\xi})$ centered at $\mathbf{r} = \boldsymbol{\xi}$ is approximated by

$$b(\mathbf{r}, \boldsymbol{\xi}) = \prod_{p=1}^{3} b\left(r^{(p)}, \xi^{(p)}\right) \tag{21}$$

with

$$b\left(x^{(p)}, \xi^{(p)}\right) = \frac{\sin\left(\frac{\pi\left(x^{(p)} - \xi^{(p)}\right)}{\Delta x^{(p)}}\right)}{N^{(p)}\Theta\left(\frac{\pi\left(x^{(p)} - \xi^{(p)}\right)}{N^{(p)}\Delta x^{(p)}}\right)} \tag{22}$$

where superscript (p) indicates the spatial dimension; $N^{(p)}$ is the grid size in dimension p; $\Delta x^{(p)}$ is the grid spacing in dimension p; and $x^{(p)}$ and $\xi^{(p)}$ are the vector components of $\mathbf{r}$ and $\boldsymbol{\xi}$, respectively. Here, $\Theta(\cdots) = \tan(\cdots)$ for even $N^{(p)}$ and $\Theta = \sin(\cdots)$ for odd $N^{(p)}$. In (22), we have omitted terms that vanish at the grid points [70].

A set of source points $\{\boldsymbol{\xi}_i\}$ with $i = 1, 2, \ldots, M$ can be represented on the discrete grid by the sum

$$s_j(t) = \sum_{i=1}^{M} C_i b\left(\mathbf{r}_j, \boldsymbol{\xi}_i\right) s\left(\boldsymbol{\xi}_i, t\right) \tag{23}$$

where $s_j(t)$ is the source signal for the jth grid point and C_i are quadrature weights [70]. In the case of microbubble sources, $C_i = (\Delta x \Delta y \Delta z)^{-1}$ and $s(\boldsymbol{\xi}_i, t) = \rho_{\mathrm{L}} \dot{V}_i(t)$, with $V_i(t)$ the volumetric oscillation of the ith microbubble (9). Similarly, we use (23) to represent an arbitrarily shaped transducer. To this end, we represent the transducer surface by a discrete set of regularly spaced integration points $\boldsymbol{\xi}_i$. In this case, $C_i = 1/A$ with A the surface area occupied by one integration point in grid units, and $s(\boldsymbol{\xi}_i, t)$ now represents the velocity vector of the oscillating transducer surface at $\boldsymbol{\xi}_i$. The same framework can be used to compute the pressure p sensed by an arbitrarily distributed set of sensor points using the equation

$$p\left(\boldsymbol{\xi}_i, t\right) = \sum_{j=1}^{N} b\left(\mathbf{r}_j, \boldsymbol{\xi}_i\right) p_j(t) \tag{24}$$

where $p_j(t)$ is the pressure sensed by the jth grid point and N is the number of grid points.

Because the band-limited delta function $b(\mathbf{x}, \boldsymbol{\xi})$ decays rapidly to negligible values with distance from the point ξ, its support can be truncated to reduce memory requirements. Empirically, we determined that a support of $9 \times 9 \times 9$ grid points, centered at the grid point closest to ξ, gives sufficiently accurate results. Fig. 6 shows the placement of sensor points on the grid for a simulation with ten microbubbles for both on-grid and off-grid cases. For a low microbubble count, the $9 \times 9 \times 9$ clusters of sensor points are largely isolated and the total number of sensor points scales linearly with the number of microbubbles. When the microbubble count increases, the number of shared sensor points increases and the total number of sensor points saturates. Fig. 6(e) visualizes the evaluated band-limited delta function for a microbubble that is midway between grid points (2-D case).

VI. Microbubble Dynamics Module

The microbubble dynamics module is an updated version of the solver presented in [28] and solves a Rayleigh–Plesset-type equation [43] to compute the nonlinear radial response $R(t)$ of each microbubble to the local driving pressure $P_{\mathrm{ac}}(t)$

$$\begin{aligned}\rho_{\mathrm{L}}\left(R\ddot{R} + \frac{3}{2}\dot{R}^2\right) &= \left[P_0 + \frac{2\sigma(R_0)}{R_0}\right]\left(\frac{R}{R_0}\right)^{-3\kappa}\left(1 - \frac{3\kappa}{c_{\mathrm{L}}}\dot{R}\right) \\ &\quad - P_0 - \frac{2\sigma(R)}{R} - \frac{4\mu\dot{R}}{R} - \frac{4\kappa_{\mathrm{s}}\dot{R}}{R^2} - P_{\mathrm{ac}}(t)\end{aligned} \tag{25}$$

where ρ_{L} is the density of the liquid surrounding the bubble, R_0 is the initial microbubble radius, $P_0 = 1.013 \times 10^5$ Pa is the ambient pressure, $\sigma(R)$ is the surface tension as a function of the radius, κ is the polytropic exponent of the gas, c_{L} is the speed of sound in the liquid, and κ_{s} is the dilational viscosity

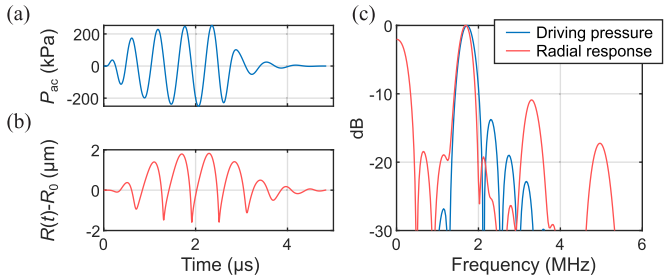

Fig. 7. Radial response of a microbubble in water. (a) Driving pressure (input microbubble module), 1.7 MHz and 250 kPa. (b) Radial excursion (output microbubble module) of a microbubble with an initial radius of 2.14 μm. (c) Frequency spectra of the driving pressure and the radial excursion of the microbubble.

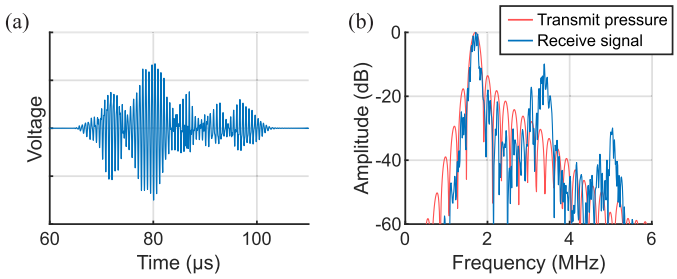

Fig. 8. (a) Backscattered signal of a 10^3 microbubbles suspension generated via the microbubble dynamics module. (b) Fourier transform of the backscattered signal shown in (a).

of the shell [71]. The quantity μ is the sum of the dynamic viscosity of the liquid μ_{vis} and a thermal damping parameter μ_{th}.

The initial microbubble radius R_0 of each microbubble is set by the microbubble trajectory module (Section IV-C). The liquid properties ρ_{L} and c_{L} are determined by the choice of vascular liquid for the acoustic module (blood or water, see Section V-B). Three options are provided to model $\sigma(R)$: 1) the Marmottant model for phospholipid-coated microbubbles [43], with its ad hoc parameters for shell elasticity and corresponding buckling and rupture points; 2) a surface tension curve from high-precision measurements by Segers et al. [71]; and 3) an arbitrary user-defined surface tension curve. The parameters μ_{th} and κ are computed with a linear theory of microbubble oscillations by Prosperetti [72] and depend on the properties of both the liquid and the gas. Three gases are predefined: hexafluoride, perfluorobutane, and perfluoropropane. When monodisperse microbubbles or BR-14 are selected as the contrast agent type (Section IV-C), the gas defaults to perfluorobutane [57], [71]. When SonoVue is selected, the gas defaults to sulfur hexafluoride [43].

The ODE (25) is solved with the MATLAB ODE45 solver. The radial oscillations $R(t)$ of each microbubble are then converted to a mass source by multiplying the volumetric rate of change $\dot{V}(t)$ by the density of the surrounding liquid ρ_{L}: $S_{\text{M}}(\mathbf{r}, t) = \rho_{\text{L}}\dot{V}(t)\delta^3(\mathbf{r}) = 4\pi\rho_{\text{L}}R^2\dot{R}\delta^3(\mathbf{r})$. This mass source is incorporated into the next iteration of the acoustic module.

Fig. 7 shows the radial excursion of a microbubble ($R_0 = 2.14$ μm) in water in response to a 1.7-MHz, 250-kPa pressure signal. For this demonstration, the experimentally measured surface tension curve was used, $\rho_{\text{L}} = 1000$ kg/m^3, $c_{\text{L}} = 1480$ m/s, $\mu_{\text{vis}} = 1$ mPa·s, $\kappa = 1$, $\mu_{\text{th}} = 0.23$ mPa·s, and $\kappa_{\text{s}} = 8.3 \times 10^{-9}$ kg/s.

VII. Results

A. RF Data From a Microbubble Population

The final output of the entire simulation pipeline of PROTEUS is RF element receive data (Fig. 1). Here, we show the RF output of a simulation of 10^3 microbubbles (radius 2.14 μm, PDI 5%) positioned in the straight pipe model in response to a long ultrasound pulse (plane-wave transmission, 8 cycles, 1.7-MHz, and 200-kPa peak negative pressure at the transducer surface, unfocused wave) transmitted with the P4-1 transducer. The center of the pipe is located at 5.8 cm from the transducer surface. To illustrate the characteristic nonlinear scatter of the microbubble population in the RF data, both the pipe and the surrounding medium are, in the acoustic module, filled with water and the nonlinearity parameter of the medium is set to zero (representing a nonphysical situation). We simulate the RF data using the semi-analytical pipeline with a grid spacing of $\lambda/8$ for the k-Wave iteration.

Fig. 8(a) shows the nonlinear backscattered time-domain signal for the central transducer element. Fig. 8(b) shows the frequency content of the backscattered signal compared to the frequency content of the transmitted pressure pulse, revealing higher harmonics generated by resonant microbubbles.

TABLE II
Tissue Properties Used in Section VII

Parameter	Symbol	Value		Unit
		Tissue	Blood	
Density	ρ_0	1000	1060	kg/m^3
Speed of sound	c_0	1540	1584	m/s
Nonlinearity parameter	B/A	6	6	
Attenuation	α_{b}	0.75	0.14	dB/MHz$^{1.5}$

B. Simulation Times of PROTEUS

We quantify the execution times of PROTEUS on a deep imaging (7.5 cm) simulation setup with a P4-1 transducer transmitting a short imaging pulse (1 cycle, 2.5-MHz, and 200-kPa peak negative pressure at the transducer surface). The propagation medium consists of soft tissue in which the renal branch is embedded. The acoustic properties of the medium are provided in Table II. The grid spacing of $\lambda/8$ results in a grid size of $1024 \times 432 \times 270$ (about 120 million grid points). We simulate both monodisperse and polydisperse microbubble populations. For the monodisperse populations, we use a Gaussian size distribution with a mean initial radius of 2.14 μm and a PDI of 5%. For the polydisperse populations, we use the distribution described in Section IV-C. The simulations are performed on a 24-GB memory GPU (Quadro RTX 6000), combined with an Intel® Xeon® Gold 5218 CPU. Note that running the simulations on CPU would result in a decrease of simulation speed by 1–2 orders of magnitude for the wave propagation simulations.

Fig. 9 shows the execution times as a function of the microbubble count, the polydispersity, the order of the microbubble–microbubble interactions, the pulsing scheme, and the employed computational pipeline. In all these cases,

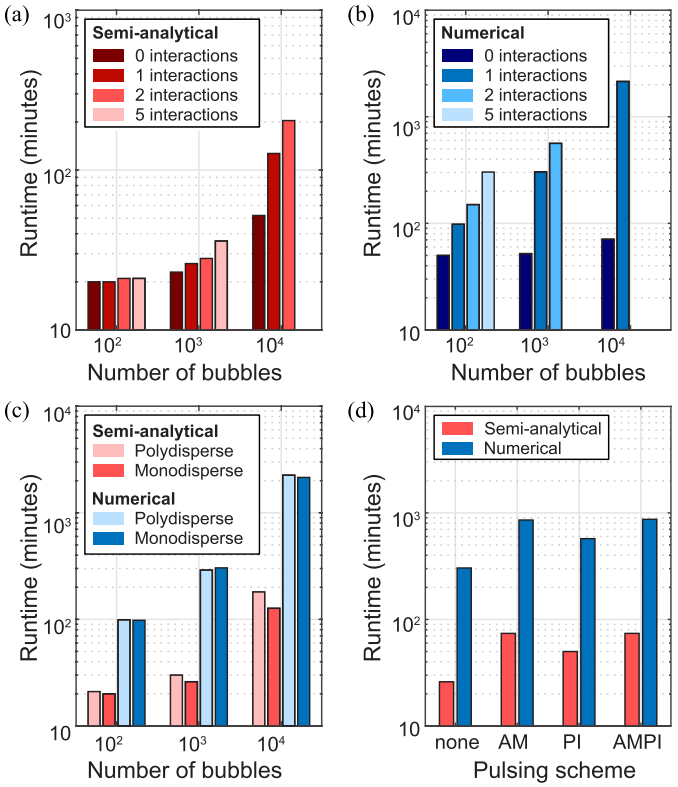

Fig. 9. PROTEUS simulation times. (a) and (b) Run times for the semi-analytical and numerical pipelines, respectively, as a function of the number of microbubbles and the order of microbubble–microbubble interactions N_{inter}. All microbubble populations are monodisperse. (c) Run times for monodisperse and polydisperse populations for both computational pipelines with $N_{\text{inter}} = 1$. (d) Run times of both pipelines for the three contrast pulse sequences with 1000 microbubbles and $N_{\text{inter}} = 1$.

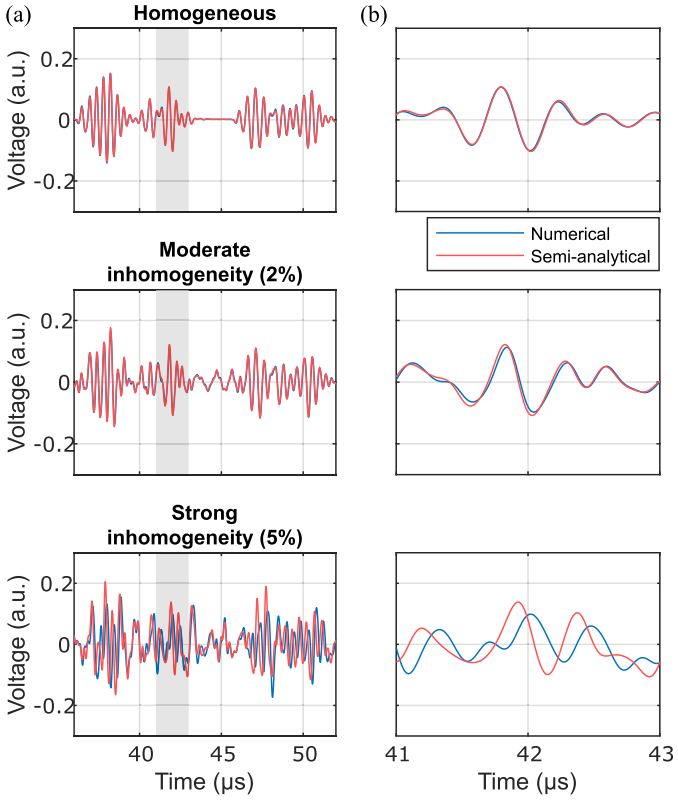

Fig. 10. Difference in backscattered signal between the numerical and the semi-analytical pipelines. (a) Difference between numerical and semi-analytical pipeline for three levels of tissue heterogeneity. Each row shows an RF channel using an AMPI scheme to suppress the background scatter. (b) Zoom on RF channels corresponding to shaded area in (a).

two frames were simulated. Therefore, the execution time for the initial k-Wave iteration [the first term in (12) and (20)] constitutes a large fraction of the total execution time. For a sufficiently high number of frames, the contribution of the initial k-Wave iteration would become negligible.

Fig. 9(a) shows that, for 10^3 microbubbles, the initial k-Wave simulation dominates the execution time. The microbubble-related computations only contribute considerably for more than 10^3 microbubbles. By contrast, Fig. 9(b) shows that the execution times for the numerical pipeline are already dominated by the microbubble–microbubble interaction computations for 100 microbubbles. This is due to the self-sense pressure computation [the term with T^{S}_{kW} in (12)] that accompanies each microbubble response computation.

Fig. 9(c) reveals that the execution time, for both pipelines, does not differ considerably between polydisperse and monodisperse populations. A slightly longer execution time can nonetheless be seen for polydisperse microbubbles due to a slightly higher value of T_{MB} in (12) and (20). The microbubble dynamics module takes longer for polydisperse populations because the ODE solver experiences increased difficulty in computing the response of the smallest microbubbles. This is related to the mismatch between the resonance frequency of the microbubble oscillation and the frequency of the pressure wave.

The use of pulse sequences [Fig. 9(d)] presents no surprises. For both pipelines, the run time scales linearly with the number of pulses, N_{p}, in the pulse sequence, in line with (12) and (20). For the PI scheme, $N_{\text{p}} = 2$. The AM and AMPI schemes are implemented using checkerboard apertures (Section V-A) with $N_{\text{p}} = 3$.

C. Comparison Numerical and Semi-Analytical Pipelines

As explained in Section V-D, the main approximation in the semi-analytical pipeline is modeling the medium as a homogeneous medium for the propagation of the microbubble scatter. In this section, we investigate the validity of that approximation. The simulation setup consists of the rat renal vasculature tree positioned at 2.5 cm from the surface of the P4-1 transducer. The tissue properties and the grid size are the same as in Section VII-B. The vasculature contains ten microbubbles with sizes drawn from the polydisperse distribution. For both the numerical and the semi-analytical pipelines, we simulate a range of tissue inhomogeneities, representing the background scatterers (Section V-B). Since, in both pipelines, the interaction between the transmitted wave and the background scatterers is simulated with a k-Wave simulation, we only expect a difference in the microbubble scatter. To suppress the background scatter, we use the AMPI pulsing scheme (2 cycles, 2.5 MHz, and 200 kPa for the full amplitude pulse).

Fig. 10 shows the outcome of the investigation. The difference between both pipelines depends, as expected, on the degree of inhomogeneity of the medium (tissue) in which the wave propagates. For each of the plots in

Fig. 10, we have computed the root-mean-square value of the difference, divided by the maximum amplitude. This yields a difference of 1% for homogeneous tissue, 3% for the moderate inhomogeneity of 2%, and a difference of 30% for the stronger inhomogeneity of 5%. The significance of this difference is application-specific. For example, the implications for reconstructed contrast mode images are explored in Part II.

Note that it would be incorrect to conclude that the numerical pipeline is necessarily more accurate than the semi-analytical pipeline. In fact, for a fully homogeneous medium, the analytical solution to the wave equation (13) is exact, whereas the k-Wave solution suffers from discretization errors. These discretization errors would be particularly pronounced in high-density microbubble populations, in which short-range microbubble–microbubble interactions cannot be accurately simulated with a spatially band-limited numerical method.

Although Fig. 10 provides insight into the limits of the semi-analytical pipeline, we cannot provide a theoretical basis for defining the level of tissue inhomogeneity that can realistically represent the background scatter in a given tissue. Moreover, for a given level of inhomogeneity, a smaller grid spacing would result in a higher intensity background scatter signal. Instead, we include the inhomogeneity level as a parameter that can be empirically tuned to match the contrast-to-tissue ratios of simulated and experimental data.

D. Reconstructed Images

Although the primary objective of PROTEUS is the generation of element RF data, we have incorporated a conventional delay-and-sum (DAS) reconstruction algorithm, partially based on methodologies published in [73], to facilitate data visualization. The RF data are first processed according to its pulse sequence (pulse-to-pulse subtraction for AM). A time-gain compensation is applied based on medium properties before applying a DAS algorithm on the Hilbert transform of the RF data. Fig. 11 shows the reconstructed images for each of the three vascular geometries presented in Fig. 2. All data were simulated with the tissue properties in Table II and without tissue scatter (tissue inhomogeneity set to zero). The microbubble sizes were drawn from the polydisperse distribution (Section IV-C).

The straight pipe [Fig. 11(a)], the rat renal vascular branch [Fig. 11(b)], and the mouse brain arteriole [Fig. 11(c)] have inlet diameters of 20 mm, 0.57 mm, and 14 μm, respectively. To resolve the decreasing scales of the vasculatures, they were imaged with transducers with increasing center frequencies (Table III). For the mouse brain arteriole ($\lambda = 86$ μm), the grid spacing was reduced from $\lambda/8$ to $\lambda/6$ to limit memory requirements.

The straight pipe is displayed with a 40-dB dynamic range and reveals all levels of signal contained in a reconstructed contrast-enhanced ultrasound image. The low-frequency speckle pattern generated by circulating microbubbles is visible in the lumen of the pipe, while bright specular reflections are visible on each wall where the transmitted wave is reflected by the interface at nearly orthogonal incidence. Curved beamforming artifacts are visible due to the limited array aperture. The rat renal vascular branch is reasonably well detected with a 5.3-MHz transmit frequency pulse, with most microbubble signal arising from the basal arteries of the branch and the tips of the branch where the microbubble concentration is higher. On the contrary, the mouse brain arteriole is not resolved since its diameter is 1/6th of the wavelength. Individual microbubble echoes are detected, however, paving the way for the implementation of ultrasound localization microscopy. In the near field of all images, the ringdown of the simulated linear transducer array is visible.

TABLE III
TRANSDUCER PROPERTIES USED FOR FIG. 11

Panel	Transducer	Number of elements	Pitch (mm)	-6 dB Frequency range (MHz)
(a)	P4-1	96	0.295	1.5 – 3.5
(b)	9L-D	192	0.23	3.3 – 7.3
(c)	L22-14v	128	0.1	14 – 22

VIII. DISCUSSION

We have presented PROTEUS, a physically accurate contrast-enhanced ultrasound simulator made up of four connected modules that simulate blood flow dynamics in segmented vascular geometries, intravascular microbubble trajectories, ultrasound wave propagation, and nonlinear microbubble scattering. This first part of this publication discusses the numerical methodologies that enabled this advancement. To our knowledge, this is the most complete framework for simulating a large amount of contrast-enhanced ultrasound RF data. We have introduced a complex flow solver and accurate modeling of microbubble behavior as well as microbubble–microbubble interactions. Because of the complexity of the simulation, we have provided two different pipelines to optimize computation costs with respect to physical accuracy. The user can fully customize each module and can choose to use our predefined vascular geometries, flows, microbubble populations, and pulse sequences or to import custom ones. To help in this regard, we have written an extensive README file that can be found here: https://github.com/PROTEUS-SIM/PROTEUS. In the next few paragraphs, we will discuss some important aspects of our work.

A. Computational Pipeline Selection

To address the needs of the scientific community, we provide two computational pipelines: a semi-analytical pipeline and a numerical pipeline. The former features accelerated simulation time by neglecting the interaction between microbubble scatter and tissue inhomogeneities, allowing the use of an analytical expression for the microbubble scatter. The latter accurately computes the propagation of ultrasound waves scattered by contrast agents through an inhomogeneous medium. However, its use is limited to microbubble populations that are sufficiently sparse to consider the finite-size voxels as point sources. In brief, the semi-analytical pipeline is ideally suited for simulating long image sequences or the acoustic response of large or dense microbubble populations. The

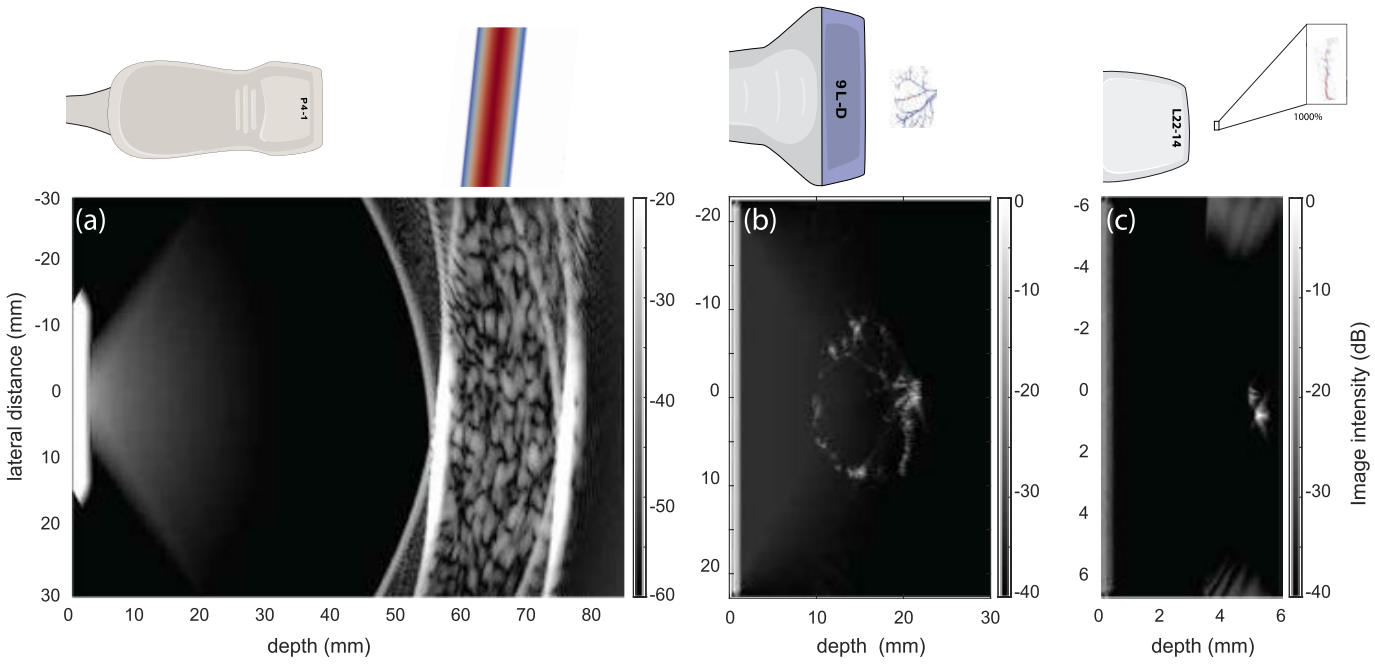

Fig. 11. Example reconstructed images (a) Macroscopic straight pipe, P4-1, 2.5 MHz, 200 kPa, and 25 000 microbubbles. (b) Rat renal vascular branch, 9L-D, 5.3 MHz, 200 kPa, and 2000 microbubbles. (c) Mouse brain arteriole, L22-14v, 18 MHz, 500 kPa, and 500 microbubbles.

numerical pipeline is best suited when the interactions between microbubble scatter and tissue cannot be neglected, either because of a strong background scatter or because of complex anatomy.

B. Memory Considerations

Currently, PROTEUS is designed to function on single-GPU platforms, making it ideally suited for widespread workstations equipped with a consumer graphics card or with single-GPU-node access in computing clusters. It has not yet been adapted to multi-GPU systems. This could, however, further speed up large simulations. Simulating a large number of bubbles (i.e., tens of thousands) for a large number of frames can place some strain on the memory. To alleviate this issue, PROTEUS allows for executing simulations in batches which, in such cases, considerably reduces the consumption of GPU memory. In order to help the user in the design of the simulation, an indication of the memory requirement is displayed in the user interface when setting the parameters.

C. Bubble-Induced Attenuation

Acoustic waves that propagate through a high-density bubble population are attenuated [55]. Currently, PROTEUS does not account for this bubble-induced attenuation. Concentrations that are too high to neglect bubble-induced attenuation are beyond the purpose of the current version.

D. Blood as a Newtonian Fluid

In the simulations presented in this work, we have modeled blood as a Newtonian fluid. The non-Newtonian nature of blood is commonly modeled with a shear-dependent viscosity, which is known to move the regions of vorticity further downstream in a flow. Furthermore, in vessels with diameters between 10 and 300 μm, the Fåhraeus–Lindqvist effect [74] becomes prominent; the apparent viscosity of blood changes due to the migration of blood cells toward the center of the vessel due to shear-induced lift forces. The renal tree and the pipe presented in PROTEUS are large enough to disregard the particulate nature of blood. Furthermore, we have not modeled microbubbles as deformable particles. Since the concentration of microbubbles is low, we can presume them to act as passive tracers. Blood cell dynamics, together with densely concentrated microbubbles, will affect the blood flow and rigid wall assumption, specifically in the brain microvasculature [75], [76], [77]. The incorporation of this complex rheological behavior and multiscale aspects has been left for future efforts.

E. Inaccessible Branches

Because of a lack of a more accurate representation, we have prescribed a zero-pressure boundary condition at all the outflows of the renal tree. In addition, some of the outlets are smaller than the surface mesh resolution and have been treated as *closed*. These boundary conditions, in addition to the presence of bifurcations and tortuosity in the vasculature, resulted in uneven flow distribution across branches, which, in turn, restricted flow in some of the smaller branches. As a result, statistically, little to no microbubbles will be present in these branches. This limitation will be overcome in future studies with a more in-depth investigation of physiological boundary conditions.

F. Non-Laminar Flow

We have performed DNS without any model for turbulence closure. Low Reynolds number and steady inflow conditions resulted in laminar flows in the three cases studied. The Reynolds number in the pipe is 5000, which is higher than the generally accepted threshold for flow transition in a pipe [78].

Nonetheless, in the absence of any perturbation or significant asymmetry in the mesh, the simulation did not transition to turbulence. All the modules within PROTEUS are, however, compatible with non-laminar flow.

G. Radiation Forces

Albeit mostly significant for long acoustic pulses, radiation forces can also have a measurable effect on the movement of microbubbles either by pushing the microbubbles through streamlines (primary Bjerknes force) or by creating an attraction or repulsion between them (secondary Bjerknes force) [54], [55]. These forces can be of interest in specific applications such as targeted drug and gene delivery [79] or ultrasound-mediated delivery of stem cells [80]. We plan on including the effect of radiation forces (together with added mass and lift forces) in a future version of PROTEUS.

H. Dynamics of Nonspherical or Confined Bubbles

The rich physics of ultrasound-driven microbubbles is still the object of intensive scientific investigation. Microbubbles exhibit a wide range of behaviors, including nonspherical oscillations [81], [82], jetting, and coalescence. As the microbubble dynamics module assumes spherical oscillations of microbubbles, it cannot fully represent all these behaviors. However, these phenomena do not play a major role at the low pressures that are common in diagnostic ultrasound.

When vessel diameters become comparable to those of the microbubbles, the microbubble dynamics can be expected to change significantly. This is currently not accounted for in the microbubble dynamics module. More advanced modeling of microbubble interactions with blood as a fluid and vessel wall such as those in [75], [76], and [77] could be included thanks to the modular nature of PROTEUS. PROTEUS also does not currently account for the interaction of individual blood cells with microbubbles.

I. Bubble Shell Models

The microbubble shell models included in the simulator are phospholipid shells since these represent the large majority of commercial agents. The simulator includes the most common model for this shell type, the Marmottant model [43], as well as a state-of-the-art shell model measured on monodisperse microbubbles [71]. Custom surface tension curves can also be loaded into the user interface to represent other formulations or to test different shell models. These custom curves can be used for ongoing investigations that aim at modifying the shell response, e.g., to boost subharmonic emission for noninvasive pressure measurement [83].

An important remark is that even the validity of the state-of-the-art models available for phospholipid shells remains limited. In particular, the dissipative effects occurring in the shell as a function of the strain rate and microbubble size are still not well understood. Furthermore, most shell models assume water as a surrounding medium and the Rayleigh–Plesset equation assumes a Newtonian liquid as the surrounding medium. However, the surface tension of blood differs from that of water. Blood also has a complex biochemical composition. Both can be expected to change the response of the microbubble. The available shell models will evolve with our knowledge of their viscoelastic properties.

Currently, PROTEUS is limited to fully reversible shell behaviors; break-up and/or plastic deformation of polymeric shells is not supported. Among the nonphospholipid shell agents, genetically encoded GVs [17] are of particular interest for emerging molecular ultrasound imaging applications. Although models for large oscillations of GVs are currently unavailable, they can be added to PROTEUS in the future.

J. Bubble Distribution in Complex Vasculature

So far, in PROTEUS, the bubbles follow the flow streamlines. Their size has therefore no effect on their trajectories. The maximum allowed bubble diameter (10 μm) only exceeds the size of the vasculature for the brain arteriole, where we advise to adjust the bubble size distribution accordingly. Nonetheless, a tool such as PROTEUS is valuable to determine the distribution of the bubbles (in terms of local concentration) in a given vasculature.

IX. Conclusion

PROTEUS is a state-of-the-art contrast-enhanced ultrasound simulator developed to generate physically realistic RF data. Its computational modules connect physically accurate flow in realistic vasculature, nonlinear wave propagation, and nonlinear microbubble physics. The various computational methods have been packaged and made publicly available.

Recognizing the various requirements of the ultrasound imaging community, we provide two alternative computational pipelines for the acoustic module: a numerical pipeline and a semi-analytical pipeline. The former handles interactions between microbubbles and tissue inhomogeneities, while the latter is fast and can handle short-range microbubble–microbubble interactions. For both pipelines, PROTEUS goes beyond discretization issues by means of a local k-space projection for both the bubbles and the transducer, making it fully suitable for high-precision applications such as super-resolution imaging.

In summary, PROTEUS is a modular, versatile, and modifiable platform that will accelerate the development and translation of new imaging strategies in the field of contrast-enhanced ultrasound. Part II of this article series reports a selection of imaging test cases to demonstrate the potential of PROTEUS.

Acknowledgment

The authors thank Charlotte Nawijn for her help on the transducer output measurements. They are grateful to Andreas Linninger for help in processing the brain microvasculature and Norman Juchler for guidance on surface mesh generation of the brain microvasculature. Kartik Jain, David Maresca, and Guillaume Lajoinie jointly supervised this work. Computing resources on the Dutch national supercomputer *Snellius* were provided by SURFSara.

REFERENCES

[1] M. Tanter and M. Fink, "Ultrafast imaging in biomedical ultrasound," *IEEE Trans. Ultrason., Ferroelectr., Freq. Control*, vol. 61, no. 1, pp. 102–119, Jan. 2014.

[2] D. Maresca et al., "Noninvasive imaging of the coronary vasculature using ultrafast ultrasound," *JACC, Cardiovascular Imag.*, vol. 11, no. 6, pp. 798–808, Jun. 2018.

[3] C. Errico, B.-F. Osmanski, S. Pezet, O. Couture, Z. Lenkei, and M. Tanter, "Transcranial functional ultrasound imaging of the brain using microbubble-enhanced ultrasensitive Doppler," *NeuroImage*, vol. 124, pp. 752–761, Jan. 2016.

[4] P. Frinking, T. Segers, Y. Luan, and F. Tranquart, "Three decades of ultrasound contrast agents: A review of the past, present and future improvements," *Ultrasound Med. Biol.*, vol. 46, no. 4, pp. 892–908, Apr. 2020.

[5] E. Stride et al., "Microbubble agents: New directions," *Ultrasound Med. Biol.*, vol. 46, no. 6, pp. 1326–1343, Jun. 2020.

[6] M. Versluis, E. Stride, G. Lajoinie, B. Dollet, and T. Segers, "Ultrasound contrast agent modeling: A review," *Ultrasound Med. Biol.*, vol. 46, no. 9, pp. 2117–2144, Sep. 2020.

[7] N. Masumoto et al., "Evaluation of malignancy grade of breast cancer using perflubutane-enhanced ultrasonography," *Ultrasound Med. Biol.*, vol. 42, no. 5, pp. 1049–1057, May 2016.

[8] K. Ferrara, P. Dayton, R. Pollard, A. Broumas, and E. Wisner, "Ultrasound imaging of tumor perfusion," *Breast Cancer Res.*, vol. 5, no. 1, Oct. 2003, Art. no. 42, doi: 10.1186/bcr701.

[9] K. Hoyt, H. Umphrey, M. Lockhart, M. Robbin, and A. Forero-Torres, "Ultrasound imaging of breast tumor perfusion and neovascular morphology," *Ultrasound Med. Biol.*, vol. 41, no. 9, pp. 2292–2302, Sep. 2015.

[10] C. Tremblay-Darveau, R. Williams, L. Milot, M. Bruce, and P. N. Burns, "Visualizing the tumor microvasculature with a nonlinear plane-wave Doppler imaging scheme based on amplitude modulation," *IEEE Trans. Med. Imag.*, vol. 35, no. 2, pp. 699–709, Feb. 2016.

[11] M. A. Averkiou, M. F. Bruce, J. E. Powers, P. S. Sheeran, and P. N. Burns, "Imaging methods for ultrasound contrast agents," *Ultrasound Med. Biol.*, vol. 46, no. 3, pp. 498–517, Mar. 2020.

[12] B. van Elburg, G. Collado-Lara, G.-W. Bruggert, T. Segers, M. Versluis, and G. Lajoinie, "Feedback-controlled microbubble generator producing one million monodisperse bubbles per second," *Rev. Sci. Instrum.*, vol. 92, no. 3, Mar. 2021, Art. no. 035110.

[13] T. Segers, A. Lassus, P. Bussat, E. Gaud, and P. Frinking, "Improved coalescence stability of monodisperse phospholipid-coated microbubbles formed by flow-focusing at elevated temperatures," *Lab Chip*, vol. 19, no. 1, pp. 158–167, 2019.

[14] T. Segers, E. Gaud, G. Casqueiro, A. Lassus, M. Versluis, and P. Frinking, "Foam-free monodisperse lipid-coated ultrasound contrast agent synthesis by flow-focusing through multi-gas-component microbubble stabilization," *Appl. Phys. Lett.*, vol. 116, no. 17, Apr. 2020, Art. no. 173701.

[15] V. G. Halldorsdottir et al., "Subharmonic contrast microbubble signals for noninvasive pressure estimation under static and dynamic flow conditions," *Ultrason. Imag.*, vol. 33, no. 3, pp. 153–164, Jul. 2011.

[16] C. Tremblay-Darveau, R. Williams, and P. N. Burns, "Measuring absolute blood pressure using microbubbles," *Ultrasound Med. Biol.*, vol. 40, no. 4, pp. 775–787, Apr. 2014.

[17] S. T. Huber, D. Terwiel, W. H. Evers, D. Maresca, and A. J. Jakobi, "Cryo-EM structure of gas vesicles for buoyancy-controlled motility," *Cell*, vol. 186, no. 5, pp. 975–986, Mar. 2023.

[18] D. Maresca et al., "Acoustic biomolecules enhance hemodynamic functional ultrasound imaging of neural activity," *NeuroImage*, vol. 209, Apr. 2020, Art. no. 116467.

[19] D. Maresca, D. P. Sawyer, G. Renaud, A. Lee-Gosselin, and M. G. Shapiro, "Nonlinear X-Wave ultrasound imaging of acoustic biomolecules," *Phys. Rev. X*, vol. 8, no. 4, Oct. 2018, Art. no. 041002.

[20] A. Matalliotakis, R. Waasdorp, M. D. Verweij, and D. Maresca, "Impact of wavefront shape on nonlinear ultrasound imaging of monodisperse microbubbles," 2024, *arXiv:2403.01452*.

[21] S. Engelhard et al., "U.S. velocimetry in participants with aortoiliac occlusive disease," *Radiology*, vol. 301, no. 2, pp. 332–338, Nov. 2021.

[22] A. M. Hoving, J. Voorneveld, J. Mikhal, J. G. Bosch, E. G. Jebbink, and C. H. Slump, "In vitro performance of echoPIV for assessment of laminar flow profiles in a carotid artery stent," *J. Med. Imag.*, vol. 8, no. 01, Jan. 2021, Art. no. 017001.

[23] J. Brum, M. Bernal, N. Barrere, C. Negreira, and C. Cabeza, "Vortex dynamics and transport phenomena in stenotic aortic models using echo-PIV," *Phys. Med. Biol.*, vol. 66, no. 5, Feb. 2021, Art. no. 055026.

[24] J. A. Jensen, S. I. Nikolov, A. C. H. Yu, and D. Garcia, "Ultrasound vector flow imaging—Part I: Sequential systems," *IEEE Trans. Ultrason., Ferroelectr., Freq. Control*, vol. 63, no. 11, pp. 1704–1721, Nov. 2016.

[25] C. Errico et al., "Ultrafast ultrasound localization microscopy for deep super-resolution vascular imaging," *Nature*, vol. 527, no. 7579, pp. 499–502, Nov. 2015.

[26] B. Heiles et al., "Ultrafast 3D ultrasound localization microscopy using a 32 × 32 matrix array," *IEEE Trans. Med. Imag.*, vol. 38, no. 9, pp. 2005–2015, Sep. 2019.

[27] R. J. G. van Sloun et al., "Super-resolution ultrasound localization microscopy through deep learning," *IEEE Trans. Med. Imag.*, vol. 40, no. 3, pp. 829–839, Mar. 2021.

[28] N. Blanken, J. M. Wolterink, H. Delingette, C. Brune, M. Versluis, and G. Lajoinie, "Super-resolved microbubble localization in single-channel ultrasound RF signals using deep learning," *IEEE Trans. Med. Imag.*, vol. 41, no. 9, pp. 2532–2542, Sep. 2022.

[29] X. Qin, J. Zhu, Z. Tu, Q. Ma, J. Tang, and C. Zhang, "Contrast-enhanced ultrasound with deep learning with attention mechanisms for predicting microvascular invasion in single hepatocellular carcinoma," *Academic Radiol.*, vol. 30, pp. S73–S80, Sep. 2023.

[30] J. A. Jensen and N. B. Svendsen, "Calculation of pressure fields from arbitrarily shaped, apodized, and excited ultrasound transducers," *IEEE Trans. Ultrason., Ferroelectr., Freq. Control*, vol. 39, no. 2, pp. 262–267, Mar. 1992.

[31] J. A. Jensen, "Field: A program for simulating ultrasound systems," Presented at the 10th Nordic-Baltic Conf. Biomed. Imag. Published Med. Biol. Eng. Comput., vol. 34, 1996, pp. 351–353.

[32] B. E. Treeby and B. T. Cox, "K-wave: MATLAB toolbox for the simulation and reconstruction of photoacoustic wave fields," *J. Biomed. Opt.*, vol. 15, no. 2, 2010, Art. no. 021314.

[33] F. Varray, A. Ramalli, C. Cachard, P. Tortoli, and O. Basset, "Fundamental and second-harmonic ultrasound field computation of inhomogeneous nonlinear medium with a generalized angular spectrum method," *IEEE Trans. Ultrason., Ferroelectr., Freq. Control*, vol. 58, no. 7, pp. 1366–1376, Jul. 2011.

[34] F. Varray, O. Basset, P. Tortoli, and C. Cachard, "CREANUIS: A nonlinear radiofrequency ultrasound image simulator," *Ultrasound Med. Biol.*, vol. 39, no. 10, pp. 1915–1924, Oct. 2013.

[35] D. Garcia, "SIMUS: An open-source simulator for medical ultrasound imaging. Part I: Theory & examples," *Comput. Methods Programs Biomed.*, vol. 218, May 2022, Art. no. 106726.

[36] I. K. Ekroll, A. E. C. M. Saris, and J. Avdal, "FLUST: A fast, open source framework for ultrasound blood flow simulations," *Comput. Methods Programs Biomed.*, vol. 238, Aug. 2023, Art. no. 107604.

[37] J. Gu and Y. Jing, "MSOUND: An open source toolbox for modeling acoustic wave propagation in heterogeneous media," *IEEE Trans. Ultrason., Ferroelectr., Freq. Control*, vol. 68, no. 5, pp. 1476–1486, May 2021.

[38] B. Heiles, A. Chavignon, V. Hingot, P. Lopez, E. Teston, and O. Couture, "Performance benchmarking of microbubble-localization algorithms for ultrasound localization microscopy," *Nature Biomed. Eng.*, vol. 6, no. 5, pp. 605–616, Feb. 2022.

[39] M. Lerendegui, K. Riemer, B. Wang, C. Dunsby, and M.-X. Tang, "BUbble flow field: A simulation framework for evaluating ultrasound localization microscopy algorithms," 2022, *arXiv:2211.00754*.

[40] H. Belgharbi et al., "An anatomically realistic simulation framework for 3D ultrasound localization microscopy," *IEEE Open J. Ultrason., Ferroelectr., Freq. Control*, vol. 3, pp. 1–13, 2023.

[41] H. Klimach, K. Jain, and S. Roller, "End-to-end parallel simulations with APES," in *Proc. Parallel Comput., Accelerating Comput. Sci. Eng. (CSE)*, vol. 25, 2014, pp. 703–711.

[42] M. Hasert et al., "Complex fluid simulations with the parallel tree-based lattice Boltzmann solver musubi," *J. Comput. Sci.*, vol. 5, no. 5, pp. 784–794, Sep. 2014.

[43] P. Marmottant et al., "A model for large amplitude oscillations of coated bubbles accounting for buckling and rupture," *J. Acoust. Soc. Amer.*, vol. 118, no. 6, pp. 3499–3505, Dec. 2005.

[44] C. K. Aidun and J. R. Clausen, "Lattice-Boltzmann method for complex flows," *Annu. Rev. Fluid Mech.*, vol. 42, pp. 439–472, Jan. 2010.

[45] M. Junk, A. Klar, and L.-S. Luo, "Asymptotic analysis of the lattice Boltzmann equation," *J. Comput. Phys.*, vol. 210, no. 2, pp. 676–704, Dec. 2005.
[46] S. Succi, R. Benzi, and F. Higuera, "The lattice Boltzmann equation: A new tool for computational fluid-dynamics," *Phys. D, Nonlinear Phenomena*, vol. 47, nos. 1–2, pp. 219–230, Jan. 1991.
[47] J. Qi, K. Jain, H. Klimach, and S. Roller, "Performance evaluation of the LBM solver musubi on various HPC architectures," in *Parallel Computing: On Road to Exascale* (Advances in Parallel Computing). IOS Press, Mar. 2016, pp. 807–816. [Online]. Available: https://ebooks.iospress.nl/volumearticle/42729
[48] K. Jain, "Efficacy of the FDA nozzle benchmark and the lattice Boltzmann method for the analysis of biomedical flows in transitional regime," *Med. Biol. Eng. Comput.*, vol. 58, no. 8, pp. 1817–1830, Aug. 2020.
[49] R. H. J. Hebbink, B. J. Wessels, R. Hagmeijer, and K. Jain, "Computational analysis of human upper airway aerodynamics," *Med. Biol. Eng. Comput.*, vol. 61, no. 2, pp. 541–553, Feb. 2023.
[50] D. A. Nordsletten, S. Blackett, M. D. Bentley, E. L. Ritman, and N. P. Smith, "Structural morphology of renal vasculature," *Amer. J. Physiol.-Heart Circulatory Physiol.*, vol. 291, no. 1, pp. H296–H309, Jul. 2006.
[51] G. Hartung et al., "Mathematical synthesis of the cortical circulation for the whole mouse brain—Part II: Microcirculatory closure," *Microcirculation*, vol. 28, no. 5, Jul. 2021, Art. no. e12687.
[52] W. Schroeder, K. Martin, and B. Lorensen, *The Visualization Toolkit*, 4th ed. New York, NY, USA: Kitware, 2006.
[53] S. Schuler, N. Pilia, D. Potyagaylo, and A. Loewe, "Cobiveco: Consistent biventricular coordinates for precise and intuitive description of position in the heart—With MATLAB implementation," *Med. Image Anal.*, vol. 74, Dec. 2021, Art. no. 102247.
[54] L. A. Crum, "Bjerknes forces on bubbles in a stationary sound field," *J. Acoust. Soc. Amer.*, vol. 57, no. 6, pp. 1363–1370, Jun. 1975.
[55] A. Prosperetti, "Bubble phenomena in sould fields: Part two," *Ultrasonics*, vol. 22, no. 3, pp. 115–124, May 1984.
[56] C. Sullivan and A. Kaszynski, "PyVista: 3D plotting and mesh analysis through a streamlined interface for the visualization toolkit (VTK)," *J. Open Source Softw.*, vol. 4, no. 37, p. 1450, May 2019.
[57] T. Segers, P. Kruizinga, M. P. Kok, G. Lajoinie, N. de Jong, and M. Versluis, "Monodisperse versus polydisperse ultrasound contrast agents: non-linear response, sensitivity, and deep tissue imaging potential," *Ultrasound Med. Biol.*, vol. 44, no. 7, pp. 1482–1492, Jul. 2018.
[58] X. Chen, K. Q. Schwarz, and K. J. Parker, "Acoustic coupling from a focused transducer to a flat plate and back to the transducer," *J. Acoust. Soc. Amer.*, vol. 94, no. 3, p. 1858, Sep. 1993.
[59] X. Chen, D. Phillips, K. Q. Schwarz, J. G. Mottley, and K. J. Parker, "The measurement of backscatter coefficient from a broadband pulse-echo system: A new formulation," *IEEE Trans. Ultrason., Ferroelectr., Freq. Control*, vol. 44, no. 2, pp. 515–525, Mar. 1997.
[60] E. Tiran et al., "Multiplane wave imaging increases signal-to-noise ratio in ultrafast ultrasound imaging," *Phys. Med. Biol.*, vol. 60, no. 21, pp. 8549–8566, Nov. 2015.
[61] B. E. Treeby, J. Jaros, A. P. Rendell, and B. T. Cox, "Modeling nonlinear ultrasound propagation in heterogeneous media with power law absorption using a K-space pseudospectral method," *J. Acoust. Soc. Amer.*, vol. 131, no. 6, pp. 4324–4336, Jun. 2012.
[62] B. E. Treeby and B. T. Cox, "Modeling power law absorption and dispersion for acoustic propagation using the fractional Laplacian," *J. Acoust. Soc. Amer.*, vol. 127, no. 5, pp. 2741–2748, May 2010.
[63] H. Azhari, "Appendix A: Typical acoustic properties of tissues," in *Basics of Biomedical Ultrasound for Engineers*. Hoboken, NJ, USA: Wiley, 2010, pp. 313–314.
[64] S. Patil and B. Ravi, "Voxel-based representation, display and thickness analysis of intricate shapes," in *Proc. 9th Int. Conf. Comput. Aided Design Comput. Graph. (CAD-CG)*, Hong Kong, 2005, pp. 415–420, doi: 10.1109/CAD-CG.2005.86.
[65] B. E. Treeby, J. Budisky, E. S. Wise, J. Jaros, and B. T. Cox, "Rapid calculation of acoustic fields from arbitrary continuous-wave sources," *J. Acoust. Soc. Amer.*, vol. 143, no. 1, pp. 529–537, Jan. 2018.
[66] J. F. Kelly, R. J. McGough, and M. M. Meerschaert, "Analytical time-domain Green's functions for power-law media," *J. Acoust. Soc. Amer.*, vol. 124, no. 5, pp. 2861–2872, Nov. 2008.
[67] T. L. Szabo, *Diagnostic Ultrasound Imaging: Inside Out*. New York, NY, USA: Academic, 2004.
[68] J. B. Keller and I. I. Kolodner, "Damping of underwater explosion bubble oscillations," *J. Appl. Phys.*, vol. 27, no. 10, pp. 1152–1161, Oct. 1956.
[69] H. Yusefi and B. Helfield, "The influence of inter-bubble spacing on the resonance response of ultrasound contrast agent microbubbles," *Ultrason. Sonochemistry*, vol. 90, Nov. 2022, Art. no. 106191.
[70] E. S. Wise, B. T. Cox, J. Jaros, and B. E. Treeby, "Representing arbitrary acoustic source and sensor distributions in Fourier collocation methods," *J. Acoust. Soc. Amer.*, vol. 146, no. 1, pp. 278–288, Jul. 2019.
[71] T. Segers, E. Gaud, M. Versluis, and P. Frinking, "High-precision acoustic measurements of the nonlinear dilatational elasticity of phospholipid coated monodisperse microbubbles," *Soft Matter*, vol. 14, no. 47, pp. 9550–9561, Dec. 2018.
[72] A. Prosperetti, "Thermal effects and damping mechanisms in the forced radial oscillations of gas bubbles in liquids," *J. Acoust. Soc. Amer.*, vol. 61, no. 1, pp. 17–27, Jan. 1977.
[73] V. Perrot, M. Polichetti, F. Varray, and D. Garcia, "So you think you can DAS? A viewpoint on delay-and-sum beamforming," *Ultrasonics*, vol. 111, Mar. 2021, Art. no. 106309.
[74] R. Fåhræus and T. Lindqvist, "The viscosity of the blood in narrow capillary tubes," *Amer. J. Physiol.-Legacy Content*, vol. 96, no. 3, pp. 562–568, Mar. 1931.
[75] C. Chen, Y. Gu, J. Tu, X. Guo, and D. Zhang, "Microbubble oscillating in a microvessel filled with viscous fluid: A finite element modeling study," *Ultrasonics*, vol. 66, pp. 54–64, Mar. 2016.
[76] J. Ri et al., "Three-dimensional numerical analysis of wall stress induced by asymmetric oscillation of microbubble trains inside microvessels," *Phys. Fluids*, vol. 35, no. 1, Jan. 2023, Art. no. 011904, doi: 10.1063/5.0134922.
[77] N. Hosseinkhah and K. Hynynen, "A three-dimensional model of an ultrasound contrast agent gas bubble and its mechanical effects on microvessels," *Phys. Med. Biol.*, vol. 57, no. 3, pp. 785–808, Jan. 2012.
[78] B. Eckhardt, T. M. Schneider, B. Hof, and J. Westerweel, "Turbulence transition in pipe flow," *Annu. Rev. Fluid Mech.*, vol. 39, pp. 447–468, Jan. 2007.
[79] J. A. Navarro-Becerra and M. A. Borden, "Targeted microbubbles for drug, gene, and cell delivery in therapy and immunotherapy," *Pharmaceutics*, vol. 15, no. 6, p. 1625, May 2023.
[80] L. Woudstra et al., "Development of a new therapeutic technique to direct stem cells to the infarcted heart using targeted microbubbles: StemBells," *Stem Cell Res.*, vol. 17, no. 1, pp. 6–15, Jul. 2016.
[81] G. Lajoinie et al., "Non-spherical oscillations drive the ultrasound-mediated release from targeted microbubbles," *Commun. Phys.*, vol. 1, 2018, Art. no. 22, doi: 10.1038/s42005-018-0020-9.
[82] H. J. Vos, B. Dollet, M. Versluis, and N. de Jong, "Nonspherical shape oscillations of coated microbubbles in contact with a wall," *Ultrasound Med. Biol.*, vol. 37, no. 6, pp. 935–948, Jun. 2011.
[83] P. A. Frinking, E. Gaud, J. Brochot, and M. Arditi, "Subharmonic scattering of phospholipid-shell microbubbles at low acoustic pressure amplitudes," *IEEE Trans. Ultrason., Ferroelectr., Freq. Control*, vol. 57, no. 8, pp. 1762–1771, Aug. 2010.